REVIEW

Check for updates

Recent advances in MOF composites for photocatalysis

Chenxi Zhang,[a] Yanhong Wu,[a] Dandan Li [ID] *[b] and Hai-Long Jiang [ID] *[c]

Metal–organic frameworks (MOFs), characterized by their tunable porosity, high surface area, and structural diversity, have emerged as promising materials for photocatalysis. To address inherent limitations of pristine MOFs such as restricted light absorption, rapid charge recombination, and insufficient active sites, MOF composites have emerged and been widely applied in photocatalysis. This review focuses on the classifications of MOF composites, emphasizing component selection and synergistic effect. Then recent environmental and energy-related photocatalytic applications are systematically discussed, including contaminant degradation, water splitting, CO_2 reduction, and N_2 fixation. Finally, the further trends and challenges of MOF composites for photocatalysis are proposed. We hope that this review can provide a forward-looking perspective on MOF composites as next-generation photocatalysts and offer actionable strategies to promote the resolution of energy crisis and environmental pollution.

[a]*Academy of Interdisciplinary Studies on Intelligent Molecules, Tianjin Key Laboratory of Structure and Performance for Functional Molecules, College of Chemistry, Tianjin Normal University, Tianjin 300387, P. R. China*

[b]*Institutes of Physical Science and Information Technology, Key Laboratory of Structure and Functional Regulation of Hybrid Materials, Ministry of Education, Anhui University, Hefei, Anhui 230601, P. R. China. E-mail: chemlidd@163.com*

[c]*Hefei National Research Center for Physical Sciences at the Microscale, Department of Chemistry, University of Science and Technology of China, Hefei, Anhui 230026, P. R. China. E-mail: jianglab@ustc.edu.cn*

1. Introduction

The escalating global energy crisis and environmental pollution demand urgent innovations in sustainable technology.[1] Photocatalysis, a change in the rate or initiation of a chemical reaction under ultraviolet, visible or infrared radiation in the presence of a light-absorbing photocatalyst that participates in reactant transformations, has emerged as a promising strategy to address these challenges by clean fuel production,[2–5] contaminant degradation,[6,7] and value-added chemical harvest.[8–10] At its core, photocatalysis relies on three sequential steps (Fig. 1): step 1, light absorption and charge carrier

Chenxi Zhang graduated from Nankai University with BSc and PhD degrees under the supervision of Prof. Shuangxi Liu in 2014 and 2019, respectively. During 2017 to 2018, he went to the University of Namur as a joint PhD student under the supervision of Prof. Bao-Lian Su. From 2019 to 2021, he worked as a joint postdoctoral researcher at the University of Science and Technology of China and Shenzhen University under the supervision of Prof. Hai-Long Jiang and Prof. Chuanxin He. He is currently an assistant research fellow at the College of Chemistry, Tianjin Normal University. His research interest focuses on photocatalysis.

Chenxi Zhang

Yanhong Wu graduated from Tianjin Normal University with a BSc degree in Chemistry in 2023. She is currently a master's student at the College of Chemistry, Tianjin Normal University. Her scientific interest focuses on photocatalysis.
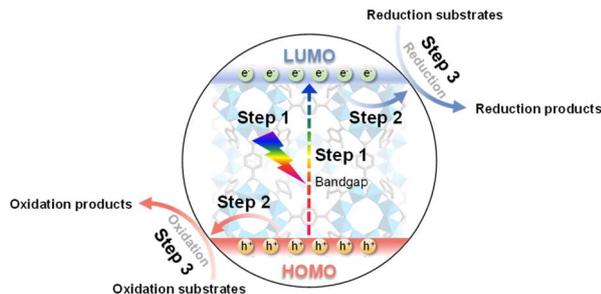
Yanhong Wu

Fig. 1 Schematic diagram of the three steps in photocatalysis.

excitation; step 2, photogenerated charge carrier separation and migration; step 3, surface catalytic reactions.[11] To enhance the overall efficiency, it is imperative to optimize each step by accordingly designing and synthesizing efficient photocatalysts. Although conventional inorganic semiconductors, such as TiO_2, CdS, and $g-C_3N_4$, have been extensively studied, their intrinsic limitations (*e.g.* the narrow light absorption range, rapid recombination and the restricted migration path of photo-generated charge carriers, and insufficient surface active sites) hinder their practical application.[12–14] These bottlenecks necessitate the development of advanced photocatalysts.

As a relatively new class of porous crystalline materials, metal–organic frameworks (MOFs) are constructed from metal ions or clusters and organic ligands.[15–20] MOFs have been widely studied in photocatalysis due to their high porosity, large specific surface area, flexible structure, easy functionalization, and diverse active sites.[21–24] Despite the above structural advantages, pristine MOFs often suffer from the limited light response range, inadequate charge mobility, and instability under certain reaction conditions, which lead to unsatisfactory photocatalytic performance.[25] To overcome these constraints, MOF composites with functional components unlock the

potential for further development in photocatalysis. Leveraging the synergistic effects, MOF composites can amplify light harvesting, suppress the recombination of charge carriers, and create additional active sites.

Currently, considerable research interest has been directed towards MOF composites in photocatalysis, as reflected in the substantial growth of related review articles. Although these reviews contribute significantly to the development of this field, they primarily focus on specific photocatalytic reactions. This review will systematically categorize MOF composites in photocatalysis based on component types and functions and spotlight the synergistic mechanisms of MOFs and components.[26–28] Then, the latest advances of MOF composites in photocatalytic reactions (*e.g.* contaminant degradation, water splitting, CO_2 reduction, and N_2 fixation) will be discussed.

Finally, critical challenges in future research will be analyzed. By correlating material design with mechanism insight, this review aims to inspire the further development of MOF composites in photocatalysis, fostering sustainable chemical production and environmental amelioration.

2. Classifications of MOF composites

To date, researchers have integrated various materials with MOFs to optimize their properties and develop novel photo-catalysts, including metal/MOF, semiconductor/MOF, reticular material/MOF, and other material/MOF. The following sections provide a comprehensive overview of these MOF composites, with particular emphasis on the functional roles of constituent components in photocatalytic processes.

2.1 Metal/MOF

Integrating metals with MOFs is one of the most efficient strategies to improve photocatalytic activity. Consequently, the

Dandan Li received her PhD degree from Anhui University in 2016 and then worked at USTC as a postdoctoral researcher under the guidance of Prof. Hai-Long Jiang from 2016 to 2018. She is currently an associate professor at Anhui University. Her research work is focused on the development of multiphoton harvesting MOFs for photocatalysis and biological applications.

Dandan Li

Hai-Long Jiang earned his PhD (2008) from the Fujian Institute of Research on the Structure of Matter, CAS. He subsequently worked at the National Institute of Advanced Industrial Science and Technology (AIST, Japan), first as an AIST Fellow and later as a JSPS Fellow during 2008–2011. After a postdoctoral stint at Texas A&M University (USA), he joined USTC as a full professor in 2013 and was appointed as a chair professor in

Hai-Long Jiang

2022. He is a Fellow of both the Chinese Chemical Society (FCCS) and Royal Society of Chemistry (FRSC) and has been annually named as a highly cited researcher by Clarivate Analytics since 2017. His research group (http://mof.ustc.edu.cn) engages in microenvironment modulation (MEM) of catalytic centers based on reticular materials.
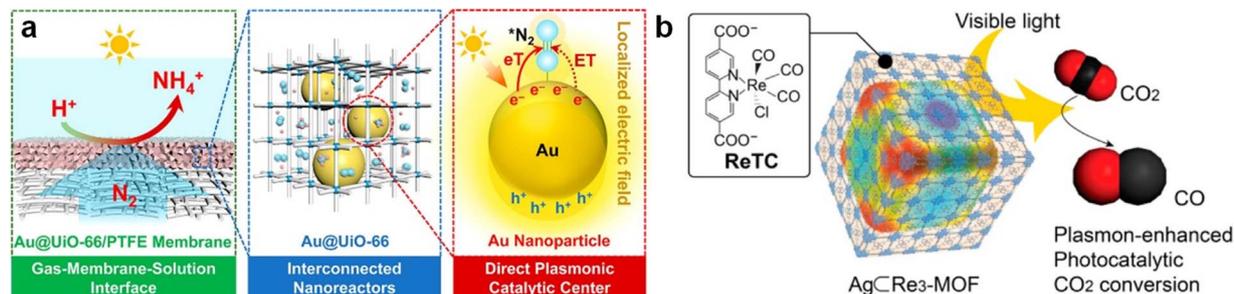
Fig. 2 (a) Schematic diagram of Au@UiO-66/PTFE membrane.[32] Copyright 2021, American Chemical Society. (b) The structure of Ag⊂Re₃-MOF for plasmon-enhanced photocatalytic CO_2 conversion.[35] Copyright 2016, American Chemical Society.

application of the resulting metal/MOF composites in photocatalysis is quite extensive.[29] According to the roles that metals play in photocatalysis, they can be broadly categorized into the following four types.

2.1.1 Introduction of the localized surface plasmon resonance (LSPR) effect. In metal nanostructures with high electron mobility (*e.g.* Au, Ag, and Cu), the LSPR effect emerges when incident light frequency matches the intrinsic oscillation frequency of valence electrons, inducing coherent electron oscillations and strong electromagnetic field amplification near metal surfaces. The LSPR effect can enhance photocatalytic performance by generating hot carriers and localized electromagnetic fields, which improves light absorption and reduces the recombination of charge carriers.[30]

In metal/MOF photocatalysts, the LSPR effect occupies an important position.[31–37] Chen *et al.* encapsulated plasmonic Au nanoparticles (NPs) within UiO-66/polytetrafluoroethylene (PTFE) membranes for photocatalytic N_2 fixation under visible light and ambient conditions (Fig. 2a).[32] The hot electrons generated on Au NPs due to the LSPR effect were injected into N_2 molecules, leading to the activation and subsequent conversion of N_2 into NH_3. The designed gas–membrane–solution interface guaranteed the stability and dispersity of Au NPs, promoting the enhancement of mass transfer of N_2 and H^+ and reaction efficiency. This strategy offers a promising approach for photocatalytic N_2 fixation and may extend to other gas molecules. Choi and coworkers integrated UiO-67 with covalently anchored Re-complex to prevent deactivation *via* dimerization (Fig. 2b).[35] By systematically tuning Re-complex density per unit cell, Re₃-MOF exhibited optimal activity due to balanced proximity between active sites. By coating on plasmonic Ag nanocubes, Re₃-MOF was spatially localized within the electromagnetic field due to the LSPR effect. Accordingly, the composite demonstrated 7-fold amplified activity and 48-hour stability in photocatalytic CO_2 reduction to CO under visible light. This work bridges tunable catalyst design within porous frameworks with plasmonic nanostructure integration for enhanced artificial photosynthesis. Xiao *et al.* developed a Cu/Cu@UiO-66 material by integrating plasmonic Cu NPs on the surface and encapsulating Cu quantum dots (QDs) within UiO-66 *via* an advanced double-solvent approach (ADSA).[37] The surface Cu NPs induced the LSPR effect to broaden the light absorption range to the visible region, while the internal Cu

QDs formed Schottky junctions with UiO-66 to facilitate charge separation, which synergistically enhanced light utilization and suppressed electron–hole recombination. The ultralow Cu loading minimized metal usage while achieving improved photocatalytic efficiency and stability in selective oxidation of benzylic alcohol.

Apart from coinage metals, other metals also participate in photocatalytic reactions due to their LSPR effect.[38] Zhang *et al.* synthesized a Bi/BiO$_{2-X}$-Bi₂O₂CO₃/BiOCl@Bi-MOF composite. The Bi-MOF provided active sites, while Bi metal improved light absorption *via* the LSPR effect.[39] The heterojunction material followed the indirect Z-scheme, which promoted charge separation and made it possible to degrade chlortetracycline (CTC) under visible light irradiation. The design emphasizes the importance of component interaction in photocatalysis.

2.1.2 Formation of the Schottky junction. For n-type semiconductors, their work functions are generally lower, or, equivalently, their Fermi levels are higher than those of metals. Upon intimate contact, the electrons on semiconductors migrate to metals to reach the equilibrium state, resulting in the formation of the Schottky junction.[40–43] The consumed electrons lead to the upward bending energy band and the depletion layer in semiconductors. The Schottky barrier is created at the interface, which favors electron capture and suppresses charge recombination. It should be noted that in the Schottky junction, the work function of the metal is required to be higher than that of the semiconductor and the flow of electrons from the metal to the semiconductor is prohibited. These characteristics are distinctly different from those of common semiconductor-cocatalyst systems in photocatalysts.

Although MOFs are not strictly semiconductors, they can form Schottky junctions with metal NPs like semiconductors as well, providing a conceptual framework for understanding interfacial charge transfer in these systems. With their previous research in mind,[44–46] the Jiang group loaded Pt NPs on MOF supports (ZIF-8, UiO-66, and MIL-125) that exhibited no visible-light response, respectively.[47] Despite being a redox-inert support with a d10 Zn^{II} configuration, ZIF-8 induced a higher Schottky barrier than redox-active UiO-66 with Zr^{IV} and MIL-125 with Ti^{IV}, which facilitated electron donation from the MOF to Pt while blocking reverse electron transfer upon visible light irradiation. Along with the Pt interband excitation, the electron density was modulated, thereby enhancing the generation of
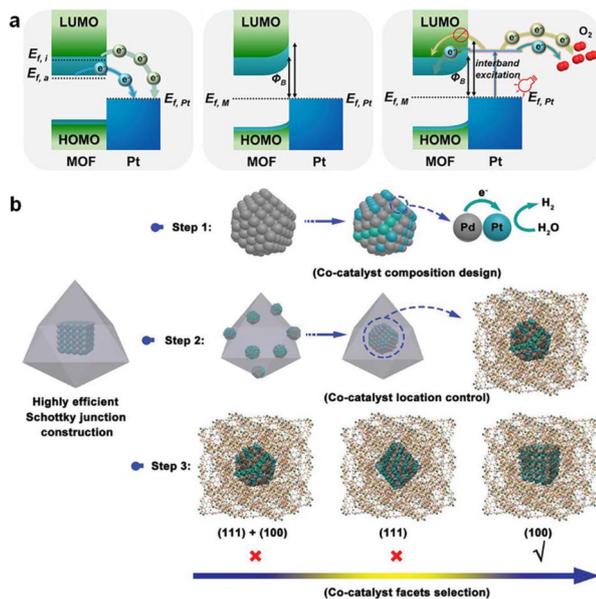
Fig. 3 (a) The electron transfer process and mechanism of Pt/MOFs. The green and cyan bands represent inert and active MOFs.[47] Copyright 2022, John Wiley and Sons. (b) The construction of a highly efficient MOF-based Schottky junction.[48] Copyright 2021, John Wiley and Sons.

reactive oxygen species $O_2^{\cdot-}$ for benzylamine oxidation over Pt/ZIF-8. In contrast, the redox-active supports permitted electron backflow, which was not conducive to the reaction (Fig. 3a). This work challenges conventional concepts and demonstrates the superiority of inert supports in optimizing metal–support electronic interactions for photocatalysis.

Taking the novel Schottky junction PtPd (100)@UiO-66-NH$_2$ as an example, Wang *et al.* proposed three parameters, $V_{transfer}$, $D_{transfer}$, and $V_{consume}$, which represent the electron transfer rate, the electron transfer distance, and the electron consume rate, respectively (Fig. 3b).[48] Through dual electron pathways, the PtPd alloy enhanced $V_{transfer}$, while encapsulation within UiO-66-NH$_2$ reduced $D_{transfer}$ by shortening the charge migration route. Exposing (100) facets of PtPd amplified $V_{consume}$ by boosting H$_2$O activation efficiency. Drawing support from the collaborative optimization of the above three strategies, the photocatalytic H$_2$ evolution rate of PtPd (100)@UiO-66-NH$_2$ was remarkably improved with a 300 W Xe lamp compared to conventional Pt/UiO-66-NH$_2$.

2.1.3 Fabrication of the Z-scheme. Mimicking natural photosynthesis, the Z-scheme photocatalysis has emerged as a highly promising system.[49–52] This two-step photoexcitation system employs two photocatalysts with staggered bandgap structures. Under light excitation, photogenerated electrons from photocatalyst II (PC II) recombine with photogenerated holes from photocatalyst I (PC I) *via* redox mediators or direct interfacial contact, leaving electrons on PC I and holes on PC II (Fig. 4a).[53] As a consequence, strong redox potentials are preserved for oxidation and reduction reactions, and the charge carriers are spatially separated. However, utilizing metal as one of the photocatalysts in a Z-scheme system is highly unusual.
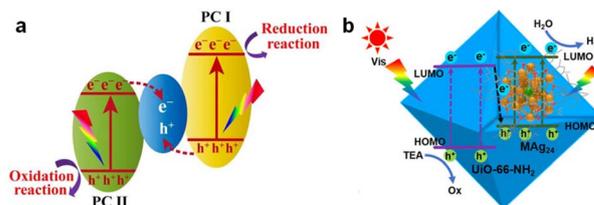

Fig. 4 (a) Schematic diagram of a Z-scheme photocatalytic system.[53] Copyright 2018, Elsevier. (b) Photocatalytic mechanism of the Z-scheme heterojunction in MAg$_{24}$@UiO-66-NH$_2$ for H$_2$ production.[54] Copyright 2024, John Wiley and Sons.

The Jiang group encapsulated atomically precise MAg$_{24}$ nanoclusters (M = Ag, Pd, Pt, Au) into UiO-66-NH$_2$ *via* electrostatic assembly.[54] As revealed by *in situ* X-ray photoelectron spectroscopy (XPS) and femtosecond time-resolved transient absorption spectroscopy (fs-TAS), heteroatom doping at the cluster core modulated charge dynamics by constructing a Z-scheme charge transfer pathway, prolonging carrier lifetimes while suppressing recombination (Fig. 4b). The metal nanoclusters were confined by UiO-66-NH$_2$, improving the stability of the composites. Among the catalysts, AuAg$_{24}$@UiO-66-NH$_2$ demonstrated optimal activity and excellent stability in photocatalytic H$_2$ production under visible light irradiation. This work pioneered a novel metal@MOF Z-scheme photocatalytic system, highlighting the critical role of atomic-level heteroatom engineering.

2.1.4 Cocatalysts. In photocatalysis, cocatalysts are widely employed to enhance charge separation and provide active sites for surface redox reactions, among which metals are one of the most common types due to their low overpotential, high electrical conductivity, and efficient electron capture ability.[55–57] In metal/MOF composites, metals often serve as cocatalysts.[58–66] The Jiang group investigated the role of cocatalyst microenvironment modulation with Pt NPs embedded in UiO-66-NH$_2$.[61] The interfacial surfactant polyvinylpyrrolidone (PVP) on Pt NPs hindered electron transfer between the MOF photosensitizer and cocatalyst. Controlled removal of PVP enhanced electrical conductivity, accelerated interfacial electron kinetics, and suppressed charge recombination, thereby improving photocatalytic H$_2$ evolution. Surface-clean Pt@UiO-66-NH$_2$ exhibited superior activity compared to the PVP-capped counterparts (Fig. 5a), which was further improved by introducing ferrocene carboxylic acid as the electron mediator. This work highlights the critical influence of interfacial microenvironments on cocatalyst functionality.

Single-atom (SA) metal cocatalysts, characterized by isolated metal atoms anchored on supports, maximize atomic utilization efficiency. Unlike conventional cocatalysts with aggregated metal NPs, the unsaturated coordination environments and highly exposed active sites of SA cocatalysts reduce energy barriers and enhance charge transfer kinetics, boosting photocatalytic activity.[67–71] Ren *et al.* anchored Ru SAs onto defective UiO-66, establishing electron–metal–support interactions (EMSI) *via* covalent bonds.[72] The EMSI facilitated rapid charge transfer between Ru SAs and UiO-66, optimizing the local
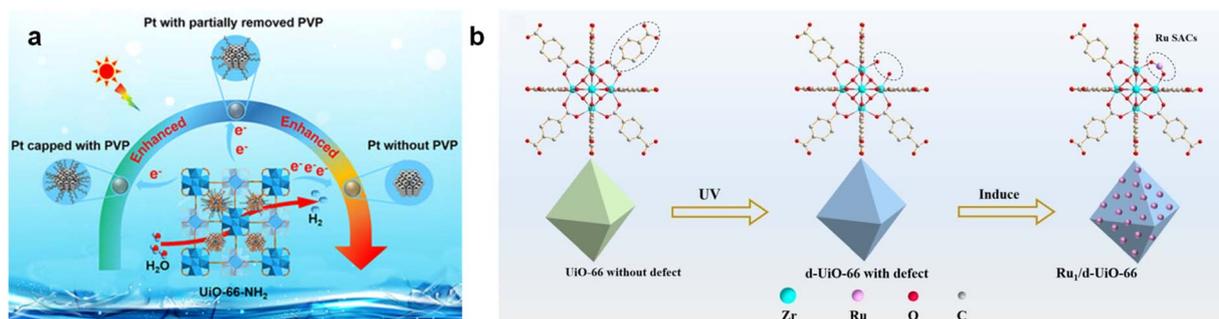
Fig. 5 (a) Schematic diagram of the photocatalytic performance of Pt@UiO-66-NH$_2$.[61] Copyright 2021, John Wiley and Sons. (b) The synthesis process of Ru$_1$/d-UiO-66.[72] Copyright 2024, John Wiley and Sons.

electron density for N$_2$ activation. Density Functional Theory (DFT) analysis revealed that Ru donated d-orbital electrons to N$_2$ π*-antibonding orbitals, weakening the N≡N triple bond. Defective UiO-66 nodes stabilized Ru SAs, preventing aggregation while redistributing electrons (Fig. 5b). The optimized Ru$_1$/d-UiO-66 exhibited enhanced photocatalytic ammonia synthesis via a distal reaction pathway under a 300 W Xe lamp. This work demonstrates the critical role of the Ru SA cocatalyst in mediating EMSI effect and activating inert N$_2$ through tailored electronic modulation.

2.2 Semiconductor/MOF

As pioneering materials in photocatalysis, semiconductors have unequivocally demonstrated their performance through decades of scientific validation. In semiconductor/MOF composites, semiconductors can significantly broaden the light absorption range and effectively enhance charge carrier separation efficiency, contributing to the improvement of photocatalytic performance.

2.2.1 Semiconductors as photosensitizers.
Due to the lack of inherent light absorption ability, certain MOFs require the

introduction of photosensitizers to facilitate photocatalytic reactions.[73,74] Jiang et al. integrated TiO$_2$ into tailored molecular compartments within MIL-101-based MOFs to optimize photocatalytic CO$_2$ reduction.[75] Acting as the light-harvesting antenna, TiO$_2$ in specific mesopores named after compartments II can synergistically interact with metal clusters embedded in MOFs, facilitating efficient electron transfer and charge separation (Fig. 6a and b). According to XPS, X-ray absorption spectroscopy (XAS), and electron paramagnetic resonance (EPR) investigations, the secondary building units (SBUs) of the MOF received electrons from TiO$_2$ to generate Cr^{2+} under light irradiation, which reverted to Cr^{3+} and evolved CO/CH$_4$ upon CO$_2$ introduction, identifying the metal containing SBUs as catalytic sites (Fig. 6c). Under a 300 W Xe lamp irradiation, the photogenerated holes on TiO$_2$ oxidized H$_2$O and evolved O$_2$ without sacrificial agent. The compartmentalized spatial control of TiO$_2$ highlights the influence of precise positioning in MOF composites.

2.2.2 Construction of type II heterojunction/Z-scheme/S-scheme.
Type II heterojunction, Z-scheme, and S-scheme systems are typical examples of heterojunctions and are familiar in semiconductor/MOF photocatalysts. Xu and
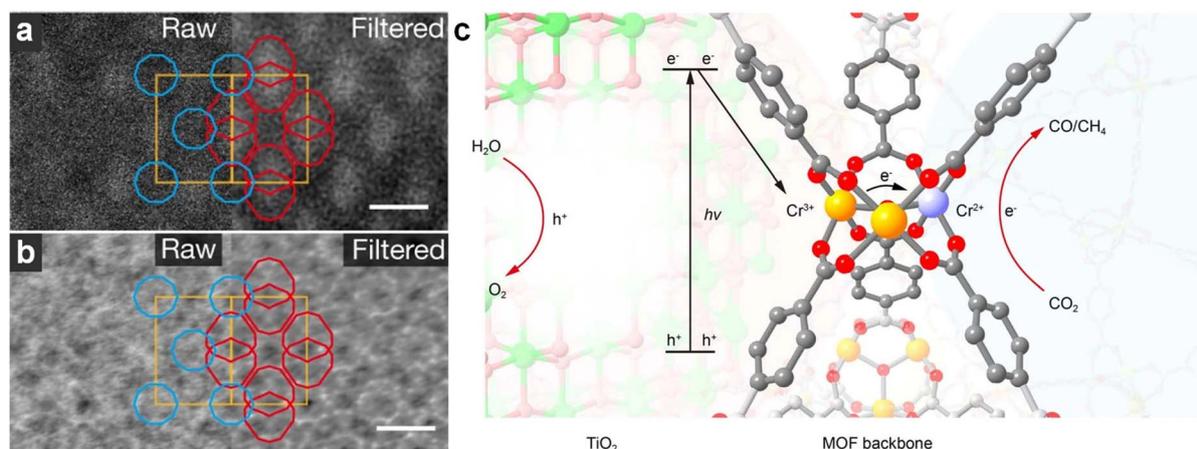
Fig. 6 Raw and filtered (a) high-angle annular dark-field (HAADF) images and (b) integrated differential phase contrast (iDPC) images of 42%-TiO$_2$-in-MIL-101-Cr taken from [110] incidence. Blue, red, and orange outlines represent compartments I, compartments II, and the unit cells, respectively. The scale bars are 5 nm. (c) Photocatalytic mechanism of TiO$_2$-in-MOF compartments composed of Cr clusters.[75] Copyright 2020, Springer Nature.
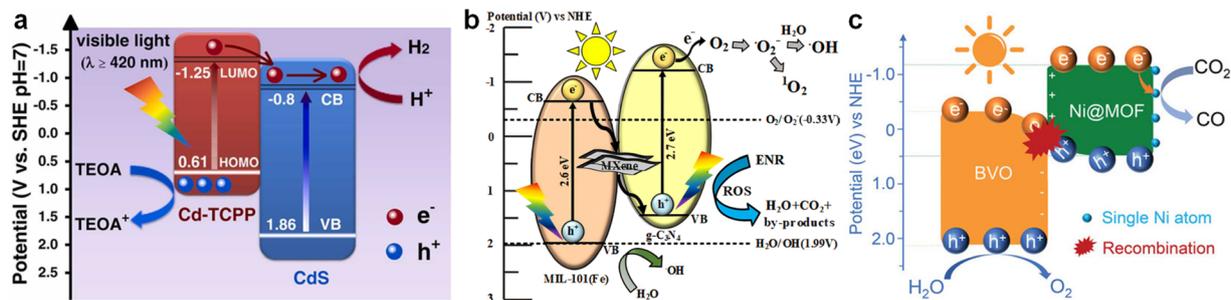
Fig. 7 (a) Photocatalytic mechanism of the type II heterojunction in CdS/Cd-TCPP for H_2 production.[76] Copyright 2022, Elsevier. (b) Photocatalytic mechanism of the Z-scheme heterojunction in MXene@g-C_3N_4/MIL-101(Fe) for ENR degradation.[77] Copyright 2025, Elsevier. (c) Photocatalytic mechanism of the S-scheme heterojunction in Ni@MOF/BVO for CO_2 reduction.[78] Copyright 2022, John Wiley and Sons.

coworkers investigated heterojunction engineering with size-controlled CdS QDs integrated with Cd-TCPP MOF nanosheets.[76] The quantum confinement effect modulated the conduction band position of CdS relative to Cd-TCPP, governing the electron injection rate across the heterojunction. Larger CdS QDs with lower conduction band potentials promoted efficient hot electron transfer while hindering light absorption. Consequently, optimal photocatalytic activity occurred at intermediate QD sizes. The type II heterojunction in CdS/Cd-TCPP enhanced H_2 production by optimizing interfacial electron transfer dynamics (Fig. 7a). This work establishes size-dependent bandgap engineering to regulate charge carrier dynamics in heterojunction photocatalysts.

Very recently, Lin *et al.* synthesized a MXene@g-C_3N_4/MIL-101(Fe) heterojunction with high surface area and abundant reactive sites for visible-light-driven photocatalytic degradation of enrofloxacin (ENR).[77] With MXene nanosheets as electron mediators, an indirect Z-scheme mechanism was established to achieve directional electron transfer from MIL-101(Fe) to g-C_3N_4 (Fig. 7b). The redox-active sites were spatially separated, thereby suppressing charge recombination. Scavenger-assisted photocatalytic degradation experiments and EPR spectral analysis demonstrated h^+ and $O_2^{\bullet-}$ as the key reactive species. The role of the Z-scheme in optimizing charge dynamics and interfacial reactions was elucidated, offering a promising way for designing MOF-based photocatalysts.

The Jing group immobilized single Ni(II) sites on 2D NTU-9 MOF, which was then assembled with $BiVO_4$ *via* H-bonds to obtain a Ni@MOF/BVO composite.[78] The heterojunction exhibited nearly 100% CO selectivity in photocatalytic reduction of CO_2, which was ascribed to the S-scheme charge transfer mechanism and the local microenvironment (LME) around Ni sites according to *in situ* diffuse reflectance infrared transform spectra (DRIFTS) and DFT calculation. The S-scheme mechanism facilitated electron migration from BVO to MOF and subsequently to single Ni(II) sites, optimizing charge separation while retaining strong redox potentials (Fig. 7c). Featuring Ti(IV)-oxo nodes and vicinal carboxylic moieties, the LME around Ni sites promoted CO_2 adsorption *via* H-bonding, proton-assisted reduction, and CO desorption, ensuring high CO selectivity (99.2%). This work emphasizes the well-designed S-scheme mechanism and single-atom catalysts with tailored

coordination environments for efficient artificial photosynthesis.

2.3 Reticular material/MOF

Reticular materials, exemplified by MOFs and covalent-organic frameworks (COFs), constitute a distinctive type of crystalline porous material. Although formed *via* coordination bonds and covalent bonds respectively, MOFs and COFs share many similarities, such as well-defined structures and high tunability.[79] The strategically designed MOF/MOF or COF/MOF composites exhibit enhanced light absorption capabilities and superior charge separation efficiency, resulting in markedly improved photocatalytic activity.

2.3.1 Reticular materials as photosensitizers. Certain MOFs or COFs exhibit excellent light absorption properties, which can complement MOFs that lack good light absorption but possess other advantages. Liu *et al.* synthesized a MOF-on-MOF composite (MIL-125@ZIF-8) through a site-selective epitaxial-growth strategy.[80] By minimizing lattice mismatch
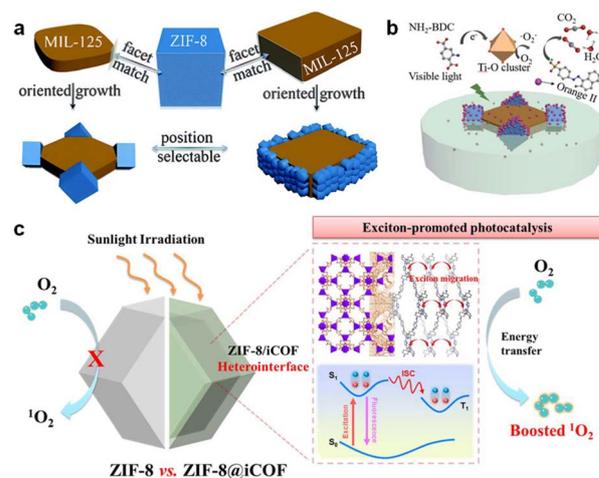

Fig. 8 (a) Schematic diagram of site-selective epitaxial-growth of ZIF-8 on MIL-125. (b) Photocatalytic mechanism of orange II degradation over ZIF-8@MIL-125.[80] Copyright 2020, Royal Society of Chemistry. (c) Photocatalytic mechanism of ZIF-8@iCOF.[81] Copyright 2023, American Chemical Society.

between {110} facets of MIL-125 and {001} facets of ZIF-8, spatially selective integration was achieved at the corner or side surface (Fig. 8a). In photocatalytic orange II degradation, ZIF-8 grown on the corner surfaces outperformed that on the side surfaces. The performance of MIL-125@ZIF-8 was remarkably enhanced owing to adsorption of dye molecules by ZIF-8 and light-harvesting property of MIL-125 (Fig. 8b), highlighting the importance of the synergistic effect of light absorption and reactant adsorption.

Similar condition also exists in ZIF-8@ionic COF (ZIF-8@iCOF) with a core–shell structure, in which iCOF acts as light antenna and generates excitons.[81] ZIF-8 effectively enhanced the intersystem crossing (ISC) of iCOF, facilitating the transfer of excitons to the lower-energy triplet excited state to produce singlet oxygen ($^1O_2$) (Fig. 8c). Under white light irradiation (50 mW cm^{-2}) for 15 min, the photocatalytic bactericidal efficiency of ZIF-8@iCOF was 99.99999%. The results provide an insightful strategy for regulating the light absorption performance of MOFs.

2.3.2 Construction of type II heterojunction/Z-scheme/S-scheme. The rational construction of heterojunctions with reticular materials has emerged as a promising strategy to promote charge carrier separation and migration efficiency. In particular, the structural tailorability of MOFs and COFs allows for precise adjustment of bandgaps and energy levels to achieve optimal band alignment.

The Jiang group explored microenvironment modulation with sandwich-structured UiO-66-NH$_2$@Pt@UiO-66-X photocatalysts.[82] By changing the functional groups (-X) of the UiO-66-X shell, both charge separation in the UiO-66-NH$_2$ core and proton reduction efficiency of the Pt mediator were synergistically regulated. According to the results of temperature-dependent photoluminescence (PL) spectra and electrochemical hydrogen evolution reaction (HER) measurements, exciton binding energy (E_b) and overpotential of UiO-66-NH$_2$@Pt@UiO-66-X were obtained to estimate the efficiencies of charge separation (η_2) and the surface reaction (η_3) (Fig. 9a). As a consequence, UiO-66-NH$_2$@Pt@UiO-66-H showed optimal activity under irradiation of >380 nm owing to the equilibrium between η_2 and η_3, highlighting microenvironment engineering as a critical strategy for coordinating photocatalytic processes.

Huang and coworkers proposed a novel method to fabricate a hierarchical core–shell PCN-222-Ni@UiO-67-NH$_2$ (P@U)

heterostructure through distinct nucleation kinetics of two Zr-MOFs.[83] Due to the structural advantages of both parent MOFs such as high crystallinity, large porosity, and good stability, the composite exhibited enhanced photoresponse, optimized band alignment, and improved charge carrier separation at the interface. Without sacrificial agents, the HCOOH production rate of P@U was 146.0 μmol g^{-1} h^{-1}, which was 2.7 times that of sole PCN-222-Ni and 8.1 times that of sole UiO-67-NH$_2$ under visible light. The EPR and *in situ* DRIFTS characterizations proved the rationality of the Z-scheme mechanism in P@U. This approach transcends conventional molecular-level optimization, emphasizing hierarchical control as a critical pathway for advanced catalyst development, which is beneficial for effective charge separation and HCOOH production.

Very recently, Chu *et al.* presented a covalently-linked MOF/COF S-scheme heterojunction NH$_2$-MIL-125/TpBpy-COF for photocatalytic overall water splitting.[84] By controlling MOF crystal facets, the anisotropic exposure of (001) and (111) facets in NH$_2$-MIL-125(Ti) enhanced the interfacial internal electric field, optimizing charge transfer *via* the S-scheme pathway (Fig. 9b). The robust built-in electric field facilitated spatial separation of photogenerated charge carriers while preserving strong redox potentials. The visible-light-driven overall water splitting H$_2$ and O$_2$ evolution rates of NH$_2$-MIL-125/TpBpy-COF were 331.6 and 165.7 μmol g^{-1} h^{-1}, which achieved the highest reported activity among COF-based photocatalysts. The work demonstrates crystal facet engineering as a reasonable strategy to strengthen S-scheme heterojunction efficiency in composite reticular materials.
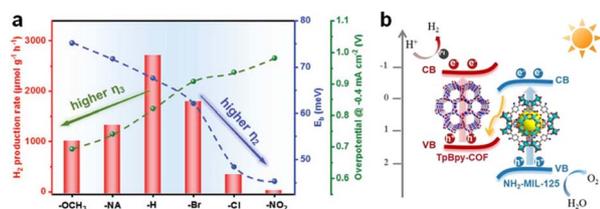
Fig. 9 (a) Photocatalytic H$_2$ production rate, E_b and overpotential in the HER of UiO-66-NH$_2$@Pt@UiO-66-X.[82] Copyright 2023, John Wiley and Sons. (b) Photocatalytic mechanism of the S-scheme heterojunction in NH$_2$-MIL-125/TpBpy-COF for overall water splitting.[84] Copyright 2025, John Wiley and Sons.
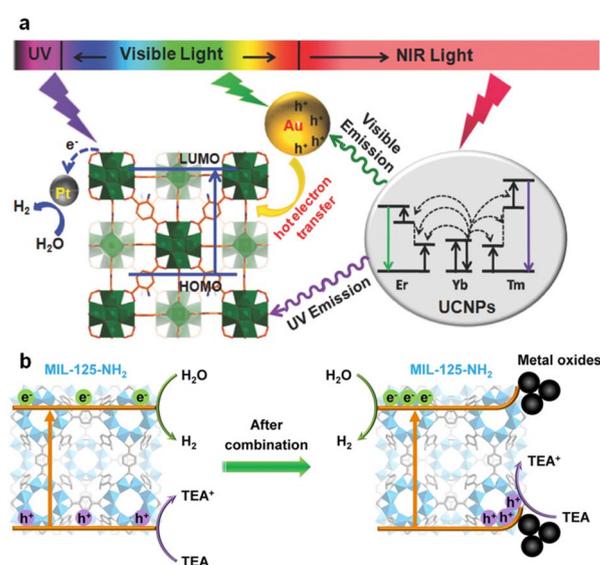
Fig. 10 (a) The light absorption region of UCNPs-Pt@MOF/Au.[87] Copyright 2018, John Wiley and Sons. (b) Schematic diagram of photocatalytic hydrogen production over MIL-125-NH$_2$ and metal oxides/MIL-125-NH$_2$.[93] Copyright 2022, John Wiley and Sons.

2.4 Other material/MOF

Beyond the aforementioned systems, it is feasible to expand MOF composites with other materials, which will be discussed as follows.

2.4.1 Upconversion nanoparticles (UCNPs)/MOF. Featuring anti-Stokes emission, UCNPs can convert long-wavelength light to short-wavelength light.[85,86] In UCNPs/MOF composites, the light absorption range of MOF is effectively broadened by UCNPs and the photocatalytic performance is enhanced. For instance, taking $NaYF_4$:Yb, Tm, Er and UiO-66-NH_2 as a core and shell respectively, the Jiang group successfully synthesized UCNPs-Pt@MOF/Au composites.[87] Due to the SPR and upconversion effects of Au and UCNPs, the composite photocatalyst can absorb all three regions, *i.e.* ultraviolet, visible, and near-infrared (NIR) regions of full solar spectrum (Fig. 10a). By adjusting the thickness of MOF and the loading amount of Au, the optimal photocatalyst presented a photocatalytic H_2 production activity of 280 $\mu mol\ g^{-1}\ h^{-1}$, and the electron transfer mechanism was clearly elucidated.

In addition to H_2 production, many reports on photocatalytic degradation with UCNPs/MOF under NIR light irradiation can be found as well.[88–92]

2.4.2 Metal oxide/MOF. Beyond serving as semiconductors, metal oxides possess the ability to regulate the charge properties of MOFs. The Jiang group integrated MIL-125-NH_2 and two metal oxides (MoO_3 or V_2O_5).[93] Unlike common semiconductors, these metal oxides possess appropriate work functions and energy levels. They neither participated in the formation of heterojunction nor acted as cocatalysts, but induced band bending in MIL-125-NH_2, which can be evidenced by a Kelvin probe force microscope (KPFM) and surface photovoltage (SPV) spectra and promoted the separation of photogenerated charge carriers. Therefore, the photocatalytic activities of the MOF composites were 56 and 42 times higher than that of pristine MOF under irradiation of >380 nm (Fig. 10b). More importantly, this is the first report on band bending in MOFs, demonstrating the semiconductor-like properties of MOFs.

2.4.3 Metal phosphide/MOF. As good electronic conductors and active sites, metal phosphides are widely recognized as excellent cocatalysts.[94–97] These unique characteristics make metal phosphides different from common semiconductors.

After integrating with MOFs, metal phosphides also demonstrate unique properties in photocatalysis. The Jiang group incorporated small, monodisperse Ni_2P with UiO-66-NH_2 for the first time.[98] The characterization revealed the electron transfer mechanism between Ni_2P and UiO-66-NH_2, demonstrating the kinetic advantage of Ni_2P over Pt (Fig. 11a). Despite leading in thermodynamics, the photocatalytic H_2 production rate of Pt@UiO-66-NH_2 was still inferior to that of Ni_2P@UiO-66-NH_2 under irradiation of >380 nm, which was the integrated result between thermodynamics and dynamics. In composites with other MOFs such as MIL-125-NH_2[99] and UiO-66,[100,101] metal phosphides also exhibited good photocatalytic H_2 production performance.

2.4.4 Carbon material/MOF. In photocatalysis, carbon materials can play various roles.[102,103] Samy *et al.* employed carbon nanotubes (CNTs) as photocatalysts and combined them with MOF-808 to obtain a heterogeneous photocatalyst for the degradation of carbamazepine and diazinon under the irradiation of 286 nm.[104] In the rational estimation, the cost of this photocatalytic system was 2.523 \$ per m^3, laying a solid foundation for its comprehensive application. Liu and coworkers synthesized a C_{60}@NU-901 composite for photocatalytic H_2 production under a 300 W Xe lamp.[105] The significant host–guest interactions between the components contributed to the formation of built-in electric fields and efficient charge separation, resulting in a remarkably improved activity. Zhou *et al.* fabricated a MIL-101/CDs-C_3N_4 composite for photocatalytic oxidative desulfurization under irradiation of >400 nm by a thermal polymerization-hydrothermal strategy.[106] The plane-averaged differential charge density plot demonstrated the formation of a Z-scheme heterojunction between MIL-101(Fe) and g-C_3N_4 (Fig. 11b). The carbon quantum dots (CDs) can capture electrons from g-C_3N_4, facilitating the separation of charge carriers. Using graphene oxide (GO) as the template and electron mediator, Wang *et al.* developed a series of ultrathin metal–organic layers (MOLs)@GO samples.[107] With
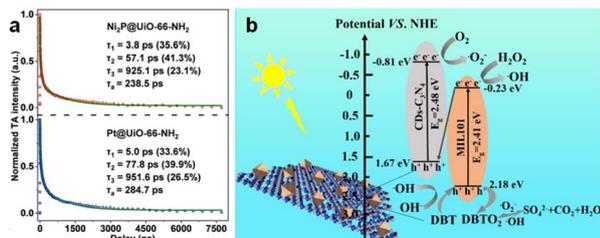
Fig. 11 (a) The transient absorption kinetics of Ni_2P@UiO-66-NH_2 and Pt@UiO-66-NH_2.[98] Copyright 2020, John Wiley and Sons. (b) Photocatalytic mechanism of the Z-scheme heterojunction in MIL101/CDs-C_3N_4 for ENR degradation.[106] Copyright 2024, John Wiley and Sons.
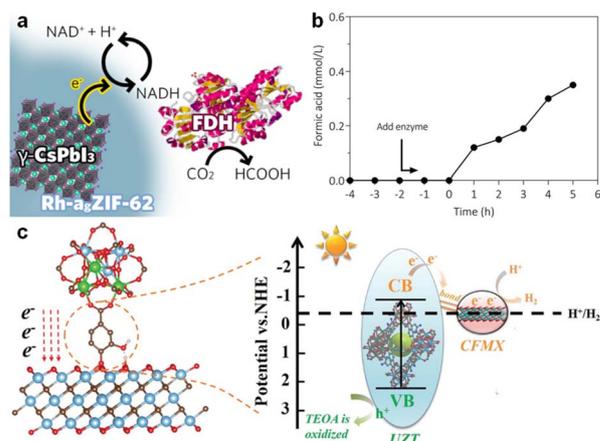
Fig. 12 (a) Photocatalytic mechanism of the artificial PS I system. (b) Time course of photocatalytic HCOOH production.[111] Copyright 2024, American Chemical Society. (c) Photocatalytic mechanism of UZT/CFMX for H_2 production.[117] Copyright 2022, John Wiley and Sons.

the help of the photosensitizer, Co-MOL@GO achieved a record-high CO evolution rate (18.0 mmol g^{-1} h^{-1}), which was 2.4 times higher than that of sole Co-MOL. The result demonstrated the importance of GO, the electron mediator. The aforementioned reports suggest that upon compositing with MOFs, different forms of carbon exhibit diverse functions in distinct photocatalytic reactions.

Table 1 MOF composites for photocatalytic contaminant degradation

| Photocatalysts	Contaminants	Light source	Activity	Ref.
UCNP/NH$_2$-MIL-125	CH$_3$CHO	Visible light	96% in 30 min	92
		Natural solar light	88% in 30 min	
		Near-infrared light	80% in 30 min	
MPA-m/U66N-m	CH$_3$COCH$_3$	350–780 nm	95% in 60 min	132
La-Bi$_2$WO$_6$-BiFeWO$_x$-WO$_3$@MOF	Phenol	≥420 nm	98.62% in 80 min	133
	Nicotine		92.41% in 80 min	
	Benzopyrene		81.74% in 80 min	
	Nitrosamine		98.23% in 80 min	
MIL-101(Fe)/ZnFe$_2$O$_4$	Phenol	300 mW LED light	99.3% in 6 min	134
MIL-101(Fe)/CQDs@g-C$_3$N$_4$	Sulfur	>400 nm	98.04% in 180 min	106
$_c$MIL-125@ZIF-8	Orange II	>420 nm	∼97.3% in 120 min	80
MIL-68@COF-V	Rhodamine 6G	Visible light	97.6% in 25 min	135
	Tetracycline		96.5% in 15 min	
	Phenols		95.3% in 40 min	
Tm@Yb@Y/NMF	Rhodamine B	300 W lamp	77% in 50 min	91
Bi$_2$MoO$_6$/MIL-88B(Fe)	Rhodamine B	420–760 nm	99.5% in 120 min	136
	Bisphenol A		54.0% in 120 min	
Sr-NDI@9,10-ME	Rhodamine B	≥420 nm	95.31% in 15 min	137
TiO$_2$@In-TCBPE	Rhodamine B	300 W lamp	100% in 13 min	138
MOF-1/GO/Fe$_3$O$_4$	Methylene blue	Visible light	95% in 80 min	139
β-NaYF$_4$:Yb,Tm/MIL-100(Fe)	Methylene blue	Full-spectrum	96.7% in 75 min	90
ZIF-8@AgNWs	Methylene blue	300–1100 nm	94% in 60 min	140
MoS$_2$@MIL-88(Fe)	Methylene blue	400–800 nm	98.5% in 60 min	141
	Rhodamine B		97.4% in 60 min	
MOF-5@rGO	Methylene blue	300–1900 nm	95% in 20 min	142
	Rhodamine B		97% in 20 min	
	Methylene orange		92% in 20 min	
CNTs/MOF-808	Carbamazepine	286 nm	91.6% in 90 min	104
	Diazinon	254 nm	99.7% in 60 min	
PDINH/MIL-88A(Fe)	Chloroquine phosphate	Visible light	95.7% in 30 min	143
Bi/BiO$_{2-X}$–Bi$_2$O$_2$CO$_3$/BiOCl@Bi-MOF	Chlortetracycline	190–1100 nm	94.6% in 90 min	39
Co/Mn-MOF-74@gC$_3$N$_4$	Doxycycline hydrochloride	>420 nm	94% in 60 min	144
MXene@g-C$_3$N$_4$/MIL-101(Fe)	Enrofloxacin	465 ± 40 nm	99% in 60 min	77
PCN-222/PCN-134	Nizatidine	Simulated visible light	90.81% in 120 min	145
γ-Fe$_2$O$_3$-MIL-53(Fe)-GO	Norfloxacin	420–780 nm	92.8% in 90 min	146
UiO-66/NH$_2$-MIL-125/g-C$_3$N$_4$	Ofloxacin	>420 nm	99.1% in 50 min	147
MIL-88A(Fe)/LaFeO$_3$	Ofloxacin	300 ± 50 mW LED light	98.4% in 10 min	148
In-MOF/BiOF	Perfluorooctanoate	500 W Hg lamp	100% in 180 min	149
TpMA@NH$_2$-MIL-125	Propylparaben	>400 nm	99% in 120 min	150
Ag/AgCl/MOF-303	Sulfamethoxazole	>420 nm	99% in 40 min	151
MIL-125-NH$_2$@CoFe PBA	Tetracycline	≥420 nm	86.9% in 120 min	152
NH$_2$-UiO-66@DAT-HOF	Tetracycline	>400 nm	∼72% in 60 min	153
MIL-125(Ti)@Ti-Ce-MOF	Tetracycline	AM 1.5G	97.8% in 30 min	154
MIL-125-NH$_2$/TiO$_2$/Ti$_3$C$_2$	Tetracycline hydrochloride	>420 nm	83% in 60 min	155
ZnIn$_2$S$_4$@PCN-224	Tetracycline hydrochloride	>420 nm	99.9% in 60 min	156
UiO-66-(COOH)$_2$/MoS$_2$/ZnIn$_2$S$_4$	Cr(VI)	500 W lamp	0.06850 min^{-1}	157
NH$_2$-MIL-88B(Fe)/CDs	Cr(VI)	Visible light	95% in 45 min	158
	Methylene blue		92% in 90 min	
UiO-66-NH$_2$@HDU-25	Cr(VI)	>420 nm	∼99% in 30 min	159
Au/MIL-101(Fe)/BiOBr	Cr(VI)	>420 nm	100% in 20 min	160
	Norfloxacin		81.8% in 75 min	
CdS-ZnS-ZIF-8	Cr(VI)	420–760 nm	99% in 10 min	161
MIL-88A(Fe)@ZnIn$_2$S$_4$	Cr(VI)	500 W lamp	100% in 9 min	162
	Sulfamethoxazole		99.6% in 60 min	
MOF525@BDMTp	U(VI)	Xe lamp	73.6% in 120 min	163
	Chlorpyrifos		99.8% in 150 min	
POM@Cu-MOFs	U(VI)	Visible light	99.4% in 60 min	164

2.4.5 Halide perovskite/MOF. Unlike common semiconductors, halide perovskites are intolerant to H_2O, which is essential in most photocatalytic reactions.[108] Therefore, encapsulating halide perovskites with MOFs for physical isolation is a feasible strategy. Kong *et al.* and Wu *et al.* fabricated $CsPbBr_3@ZIF-67$ and $MAPbI_3@PCN-221(Fe_x)$ respectively, achieving photocatalytic reduction of CO_2 to CH_4 and CO.[109,110] Inspired by the thylakoid membrane, Huang and coworkers mimicked natural photosystem I (PS I) and introduced $CsPbI_3$ into Rh-functionalized ZIF-62 MOF glass to construct a novel artificial photosynthesis system.[111] Through liquid-phase sintering at 325 °C under argon protection, the light absorption range was broadened to 600–800 nm and the surface defects of $CsPbI_3$ were passivated. In addition, an alloyed interface between the components was formed, benefiting the extraction and transfer of photogenerated charge carriers. Under visible light irradiation, the coenzyme nicotinamide adenine dinucleotide (NADH) was first regenerated over the composite catalyst. Then the derived protons and electrons were transferred to formate dehydrogenase (FDH), reducing CO_2 to HCOOH (Fig. 12a). The HCOOH production rate of the tandem reaction was ~0.12 mmol h^{-1} within 1 hour and ~0.07 mmol h^{-1} within 5 hours with nearly 100% selectivity (Fig. 12b). This work highlights the synergistic role of MOFs and halide perovskites, offering a novel design for sustainable solar-driven chemical synthesis.

2.4.6 MXene/MOF. MXenes refer to transition metal carbides, nitrides, or carbonitrides with two-dimensional structures.[112–114] Thanks to their low Fermi level and high electrical conductivity, MXenes often serve as efficient cocatalysts in photocatalysis.[115] The Huang group synthesized $Ti_3C_2@MIL-125-NH_2$ by an *in situ* growth method, in which Ti_3C_2 acted as the Ti source.[116] In photocatalytic H_2 production under AM 1.5G light, the cocatalyst Ti_3C_2 facilitated the transfer of excited electrons on $MIL-125-NH_2$ through Ti–N bonds, promoting the reduction of H^+ to H_2. Shi *et al.* constructed a novel UiO-66-NH_2(Zr/Ti)/carboxyl-functionalized MXene (UZT/CFMX) photocatalyst *via* the carboxyl-assisted coordination strategy.[117] The heterojunction suppressed the recombination of charge carriers and mediated H_2O activation through carbon (from the carboxyl group)-oxygen (from H_2O) interaction (Fig. 12c). Therefore, additional pathways for photocatalytic water splitting were created. The synergistic interactions optimized the interfacial reaction dynamics and collectively boosted the photocatalytic activity under 350–780 nm irradiation. The semiconductor characteristics of MXenes also allow the construction of heterostructures between them and MOFs.[118] For instance, a 0D/2D Ti_3C_2 quantum dots/two-dimensional nickel-MOF (Ti_3C_2-QDs/Ni-MOF) heterojunction composite was reported by Qin and coworkers for photocatalytic N_2 fixation under a 300 W Xe lamp.[119] The internal electric field formed between the components accelerated the migration of photogenerated electrons, and Ti_3C_2-QDs significantly promoted the physical adsorption of N_2, which was the prerequisite for the reaction.

3. Applications of MOF composites in photocatalysis

This section will systematically examine representative applications of MOF composites in photocatalysis, including contaminant degradation, water splitting, CO_2 reduction, and N_2 fixation. To capture the most recent developments, our coverage focuses on reports published after 2020.

3.1 Contaminant degradation

Water pollution has emerged as a critical global challenge, which poses a severe threat to the environment and human health due to the persistence and toxicity of contaminants.[120–123] Photocatalysis, a sustainable technology utilizing light energy to drive redox reactions, offers a promising solution for contaminant degradation by converting hazardous substances into harmless products.[124–127] Combining the exceptional adsorption capability of MOFs with the functionality of nanomaterials, MOF composites have attracted attention for contaminant degradation recently (Table 1),[128–131] including volatile organic compounds (VOCs), dyes, antibiotics, and heavy metals.

Shah *et al.* integrated NH_2-BDC stabilized NaYbF4:Tm^{3+} (UCNP) and NH_2-MIL-125(Ti) to form UCNP/NMIL(Ti).[92] Under visible/solar/NIR light, UCNP/NMIL(Ti) can degrade 96%/88%/80% of VOC CH_3CHO in 30 min with apparent rate constants 3.4/2.5/2.4-fold those of UCP@NMIL(Ti), in which NaYbF4:Tm^{3+} was stabilized with EDTA instead of NH_2-BDC. The results undoubtedly proved the significance of the ligand-sharing synthetic method. The degradation efficiency exhibited a positive correlation with relative humidity (0–100% RH), suggesting rapid conversion of H_2O to ·OH radicals (Fig. 13a). Moreover, the excellent photocatalytic performance can be attributed to abundant oxygen vacancies, coordinatively unsaturated metal
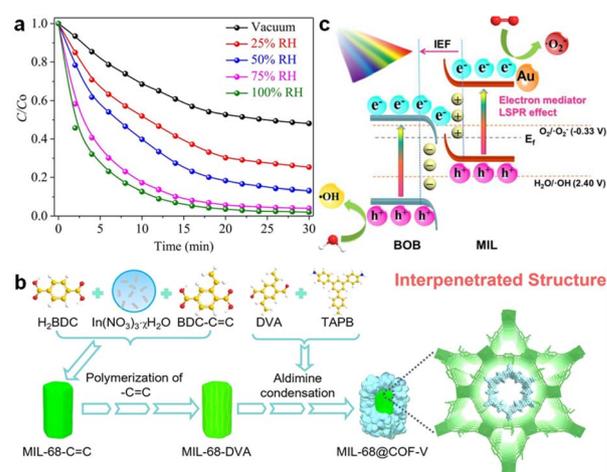

Fig. 13 (a) Photocatalytic CH_3CHO degradation rate curves over UCNP/NMIL(Ti) under visible light with different RH%.[92] Copyright 2022, Elsevier. (b) The construction process of MIL-68@COF-V.[135] Copyright 2024, John Wiley and Sons. (c) Photocatalytic mechanism of the plasmonic S-scheme heterojunction in Au/MIL/BOB.[160] Copyright 2024, Elsevier.

Table 2 MOF composites for photocatalytic water splitting

Photocatalysts	SA[a]	Cocatalysts	Light source	Products	Activity	AQE[b]	Ref.
PtPd cubes@UiO-66-NH$_2$	Trolamine	—	300 W lamp	H$_2$	6.97 μmol h^{-1}	—	48
Au/PFC-9	Trolamine	—	400–800 nm	H$_2$	130 μmol g^{-1} h^{-1}	0.009%@400 nm	33
AuPt@UiO-66	Triethylamine	—	300 W lamp	H$_2$	340.2 μmol g^{-1} h^{-1}	5.01%@550 nm	65
CoMo$_6$S$_{24}$@NU1K	Trolamine	—	=390 nm	H$_2$	360 μmol g^{-1} h^{-1}	—	170
MoO$_3$/MIL-125-NH$_2$	Triethylamine	—	>380 nm	H$_2$	399.0 μmol g^{-1} h^{-1}	0.41%@380 nm	93
Ni$_2$P@UiO-66-NH$_2$	Triethylamine	—	>380 nm	H$_2$	409.1 μmol g^{-1} h^{-1}	—	98
TiO$_2$@NH$_2$-MIL-125(Ti)	Trolamine	—	AM 1.5G	H$_2$	440 μmol g^{-1} h^{-1}	—	171
Cu-NH$_2$-MIL-125	Triethylamine	—	=420 nm	H$_2$	490 μmol g^{-1} h^{-1}	6.6%@420 nm	172
Pt-Fc@UiO-66-NH$_2$	Trolamine	—	>380 nm	H$_2$	514.8 μmol g^{-1} h^{-1}	—	61
Au@NH$_2$-UiO-66/CdS	Lactic acid	—	>420 nm	H$_2$	664.9 μmol g^{-1} h^{-1}	5.1%@400 nm	173
Pd@Pt/UiO-66-NH$_2$	Triethylamine	—	>380 nm	H$_2$	1200.5 μmol g^{-1} h^{-1}	—	46
Zr-MOF-S@CdS	Lactic acid	Pt	≥420 nm	H$_2$	1861.7 μmol g^{-1} h^{-1}	—	174
Cs$_{2.5}$H$_{0.5}$PW$_{12}$O$_{40}$@ UiO-66-NH$_2$(Hf-Zr)	Trolamine	—	>420 nm	H$_2$	1822 μmol g^{-1} h^{-1}	—	175
Cu-MOL/Ni-MOL	Ascorbic acid	—	≥400 nm	H$_2$	2027 μmol g^{-1} h^{-1}	2.75%@420 nm	176
UiO-66-NH$_2$(Zr/Ti)/MXene	Trolamine	Pt	350–780 nm	H$_2$	2187 μmol g^{-1} h^{-1}	—	117
NH$_2$-MIL-125(Ti)@ZnIn$_2$S$_4$/CdS	CH$_3$OH	—	>400 nm	H$_2$	2.367 mmol g^{-1} h^{-1}	—	177
CdS/Ni-MOF	Lactic acid	—	>420 nm	H$_2$	2508 μmol g^{-1} h^{-1}	13.03%@450 nm	178
p-TCN@U6-3	Trolamine	—	>420 nm	H$_2$	2628 μmol g^{-1} h^{-1}	—	179
UiO-66-NH$_2$@Pt@UiO-66-H	Triethylamine	—	>380 nm	H$_2$	2708.2 μmol g^{-1} h^{-1}	—	82
CdS/Cd-TCPP	Trolamine	—	≥420 nm	H$_2$	3150 μmol g^{-1} h^{-1}	—	76
AuAg$_{24}$@UiO-66-NH$_2$	Triethylamine	—	>380 nm	H$_2$	3.6 mmol g^{-1} h^{-1}	0.53%@380 nm	54
Ni-Sb$_9$@UiO-Ir-C6	BIH[c]	—	>420 nm	H$_2$	4.3 mmol g^{-1} h^{-1}	—	180
Ti$_3$C$_2$@MIL-NH$_2$	Trolamine, CH$_3$OH	—	AM 1.5G	H$_2$	4383.1 μmol g^{-1} h^{-1}	3.14%@420 nm	116
Pt(1.5)/MIL-125-NH-CH$_2$OH	Trolamine	—	>420 nm	H$_2$	4496.4 μmol g^{-1} h^{-1}	—	62
S-NRs/NMOF-Ni	Lactic acid	—	300 W lamp	H$_2$	4500 μmol g^{-1} h^{-1}	11.83%@365 nm	181
Ni-MOF-74/BiVO$_4$/P	Trolamine	—	≥420 nm	H$_2$	4908 μmol g^{-1} h^{-1}	—	182
ZnIn$_2$S$_4$-NiO@MOF	Trolamine	—	≥420 nm	H$_2$	4970.9 μmol g^{-1} h^{-1}	5.91%@405 nm	183
CoPOH/MIL	Triethylamine	—	>385 nm	H$_2$	6.6 mmol g^{-1} h^{-1}	11.4%@390 nm	184
NH$_2$-UiO-66@TFPT-DETH	Sodium ascorbate	Pt	≥420 nm	H$_2$	7178 μmol g^{-1} h^{-1}	1.11%@420 nm	185
CdS/P415-NH$_2$	Na$_2$S and Na$_2$SO$_3$	—	>420 nm	H$_2$	138 μmol g^{-1} min^{-1}	8.2%@420 nm	186
NU-1000@ZnIn$_2$S$_4$	Trolamine	—	≥400 nm	H$_2$	8.53 mmol g^{-1} h^{-1}	5.9%@380 nm	187
CdS@MOF-808	Triethylamine	—	>420 nm	H$_2$	10.41 mmol g^{-1} h^{-1}	3.28%@400 nm	188
ZnCo$_2$S$_4$/MOF-199	Trolamine	—	>420 nm	H$_2$	11.6 mmol g^{-1} h^{-1}	4.92%@420 nm	189
HKUST-1/TiO$_2$	CH$_3$OH	—	300 W lamp	H$_2$	13.25 mmol g^{-1} h^{-1}	—	190
MTV-Ti-MOF/COF	Ascorbic acid	Pt	>420 nm	H$_2$	13.98 mmol g^{-1} h^{-1}	5.9%@515 nm	191
NH$_2$-MIL-125(Ti)/Zn$_{0.5}$Cd$_{0.5}$S/NiS	Trolamine	Pt	>420 nm	H$_2$	14 876.7 μmol g^{-1} h^{-1}	24.2%@420 nm	192
20% H$_2$N-Cu-MOF/TpPa-1-COF	Ascorbic acid	Pt	≥420 nm	H$_2$	15.3 mmol g^{-1} h^{-1}	0.72%@420 nm	193
Pt-SAs@Pd-PCN-222-NH$_2$	TIPA[d]	—	≥420 nm	H$_2$	16 591 μmol g^{-1} h^{-1}	—	194
UiO-66-(COOH)$_2$/MoS$_2$/ZnIn$_2$S$_4$	Na$_2$S and Na$_2$SO$_3$	—	300 W lamp	H$_2$	18.794 mmol g^{-1} h^{-1}	—	157
CdS@PCN-222(Pt)	Lactic acid	—	≥420 nm	H$_2$	29.5 mmol g^{-1} h^{-1}	9.9%@420 nm	195
C$_{60}$@NU-901	Ascorbic acid	Pt	300 W lamp	H$_2$	22.3 mmol g^{-1} h^{-1}	0.45%@420 nm	105
ZCS-0.5/MOF-545Co	Lactic acid	—	=420 nm	H$_2$	29.6 mmol g^{-1} h^{-1}	—	196
Au@UiOS@ZnIn$_2$S$_4$	Na$_2$S and Na$_2$SO$_3$	—	420–780 nm	H$_2$	39.16 mmol g^{-1} h^{-1}	30.1%@365 nm	197
UiOS-Cu-CdS/ZnS	Na$_2$S and Na$_2$SO$_3$	—	320–780 nm	H$_2$	42.55 mmol g^{-1} h^{-1}	20.2%@400 nm	198
CuSL-CuBr	Triethylamine	—	420–800 nm	H$_2$	50.28 mmol g^{-1} h^{-1}	0.47%@500 nm	199
ZnIn$_2$S$_4$@PCN-224	Na$_2$S and Na$_2$SO$_3$	Pt	>420 nm	H$_2$	68.2 mmol g^{-1} h^{-1}	6.45%@420 nm	156
Liposome-MOF	—	Pt, Ir	400 and 450 nm	H$_2$ and O$_2$	H$_2$: 11.6 μmol g^{-1} h^{-1}; O$_2$: 6.4 μmol g^{-1} h^{-1}	(1.5 ± 1)%@436 nm	200
Pt@NH$_2$-UiO-66@MnO$_x$	—	—	≥400 nm	H$_2$ and O$_2$	H$_2$: 19.6 μmol g^{-1} h^{-1}; O$_2$: 10.1 μmol g^{-1} h^{-1}	—	60
Fe$_2$NiCbz-P33	—	—	≥420 nm	H$_2$ and O$_2$	H$_2$: 170.2 μmol g^{-1} h^{-1}; O$_2$: 85.1 μmol g^{-1} h^{-1}	∼1.3%@595 nm	201
NH$_2$-MIL-125(Ti)/TpBpy-COF	—	Au, MnO$_x$	>420 nm	H$_2$ and O$_2$	H$_2$: 331.6 μmol g^{-1} h^{-1}; O$_2$: 165.7 μmol g^{-1} h^{-1}	6.06%@450 nm	84
CdS@ZIF	—	—	≥400 nm	H$_2$ and O$_2$	H$_2$: 346.8 μmol g^{-1} h^{-1}; O$_2$: 173.4 μmol g^{-1} h^{-1}	1.77%@400 nm	202

[a] Sacrificial agents. [b] Apparent quantum efficiency. [c] 2,3-Dihydro-1,3-dimethyl-2-phenyl-1H-benzimidazole. [d] Triisopropanolamine.

sites, broad light absorption range, and high charge carrier separation efficiency. This work provides new possibilities for exploring novel synthetic strategies.

Zhou and coworkers introduced a novel C–C covalent linkage strategy to construct a core–shell MIL-68@COF-V composite (Fig. 13b).[135] Unlike imine-linked MIL-68-NH$_2$@COF-V, MIL-68@COF-V possessed adjustable shell thickness and the interpenetrated structure, resulting in enhanced light absorption and charge carrier separation. Under visible light, MIL-68@COF-V exhibited a comprehensive degradation effect on dye (rhodamine 6G), antibiotic (tetracycline), and VOC (phenol), far exceeding MIL-68-NH$_2$@COF-V. Furthermore, the *in situ* growth MIL-68@COF-V film degraded 97.6% of rhodamine 6G in 25 min, 96.5% of tetracycline in 15 min, and 95.3% of phenol in 40 min, with apparent rate constants 1.61–2.86 times as high as those of the powder composite. This work highlights the potential of C–C covalently linked MOF@COF heterostructures through rational structure design and scalable film fabrication.

Simultaneous photocatalytic degradation of heavy metals and antibiotics faces limitations in terms of active sites, charge separation, and redox ability. In the work reported by Li *et al.*, a novel plasmonic S-scheme heterojunction Au/MIL-101(Fe)/BiOBr (Au/MIL/BOB) was constructed *via* a solvothermal-photoreduction method (Fig. 13c).[160] Compared to pristine BiOBr, the visible-light-driven photocatalytic degradation apparent rate constants of the optimized catalyst were enhanced by 53.3 and 2 times for Cr(VI) and norfloxacin (NOR), respectively. The synergistic effect in the Cr(VI)-NOR system effectively increased the carrier utilization. Due to the LSPR effect of Au NPs, the light absorption of Au/MIL/BOB was promoted. The MOF-based S-scheme structure facilitated the separation of charge carriers and the exposure of active sites, while maintaining high redox ability. The rational design of Au/MIL/BOB demonstrates great potential in wastewater purification.

3.2 Water splitting

As a sustainable and eco-friendly energy source, H$_2$ has garnered significant attention in recent years.[165] Photocatalytic water splitting has emerged as a competitive approach for H$_2$ production,[166,167] with MOF composites demonstrating remarkable potential in this field.[168,169] A summary of MOF composites for photocatalytic water splitting is presented below (Table 2). It should be noted that based on reaction products, photocatalytic water splitting with MOF composites can be categorized into two types: H$_2$ production exclusively with sacrificial agents and overall water splitting H$_2$ and O$_2$ production simultaneously without sacrificial agents. Most research in the table still focuses on H$_2$ production, while progress in overall water splitting remains relatively limited, with activity yet to be improved. This is primarily due to the difficulty in overcoming the slow kinetics of the water oxidation reaction.

A hierarchical ZnIn$_2$S$_4$@PCN-224 composite was integrated by Jin *et al.* through a facile solvothermal method.[156] The optimized composite demonstrated an exceptional visible-light-
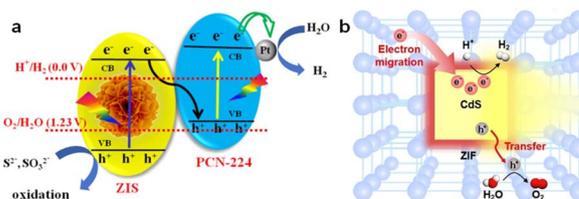

Fig. 14 (a) Photocatalytic mechanism of the Z-scheme heterojunction in ZnIn$_2$S$_4$@PCN-224.[156] Copyright 2021, Elsevier. (b) Photocatalytic mechanism of CdS@ZIF.[202] Copyright 2023, John Wiley and Sons.

driven photocatalytic water splitting H$_2$ production rate, achieving 5.68 mmol g^{-1} h^{-1} without cocatalyst. With Pt cocatalyst loaded by the *in situ* growth method, the H$_2$ production rate boosted to 68.2 mmol g^{-1} h^{-1}, surpassing those of most MOF composites. Structural and mechanistic analyses revealed that the enhanced activity stemmed from the effective Z-scheme heterojunction in ZnIn$_2$S$_4$@PCN-224, which facilitated spatial separation of electron–hole pairs while maintaining strong redox potentials (Fig. 14a). Hierarchical architecture not only enhanced charge carrier dynamics, but also provided abundant active sites.

Ng and coworkers exploited the multifunctional interface between CdS and ZIF-8 (CdS@ZIF) to achieve overall water splitting under irradiation of ≥400 nm.[202] In the absence of sacrificial agent and cocatalyst, the optimal H$_2$ and O$_2$ production rates of CdS@ZIF were 346.8 and 173.4 μmol g^{-1} h^{-1} with an ideal stoichiometric ratio of 2 : 1. The interface can enrich the photogenerated electrons on CdS to promote H$_2$ production and delocalize photogenerated holes to ZIF to boost O$_2$ production (Fig. 14b). Mechanistic analyses revealed that the intelligently designed interface enhanced the intrinsic catalytic activity of CdS and improved the intrinsic catalytic activity of CdS and improved the transfer and utilization efficiency of charge carriers.

The above reports illustrate the high value of component selection and mechanism research in MOF composites.

3.3 CO$_2$ reduction

As a kind of greenhouse gas, CO$_2$ exacerbates global warming, extreme weather, and ocean acidification, which threatens ecosystems and biodiversity.[203–205] Photocatalysis is a promising strategy to reduce CO$_2$ to fuels or chemicals and achieve sustainable carbon cycling.[206,207] Among various photocatalysts, MOF composites have demonstrated exceptional potential due to their prominent CO$_2$ capture capabilities.[208,209] The following is a summary of the research reports on photocatalytic CO$_2$ reduction with MOF composites (Table 3).

According to the carbon chain length, CO$_2$ reduction products can be primarily categorized into single-carbon (C$_1$) products (*e.g.* CO, CH$_4$, CH$_3$OH, and HCOOH) and multi-carbon (C$_{2+}$) products (*e.g.* C$_2$H$_6$ and CH$_3$COOH). One example of each category will be given below.

Very recently, Cai and coworkers presented an In-based MOF heterostructure In-NH$_2$-MIL-68@In-TCPP (M68N@In-TCPP) *via* one-pot synthesis.[210] The core–shell architecture integrated the

Table 3 MOF composites for photocatalytic CO_2 reduction

Photocatalysts	Photosensitizers	SA[a]	Light source	Products	Selectivity	Activity	AQE[b]	Ref.
$Cu_2O@Cu_3(BTC)_2$	—	—	>400 nm	CH_4	—	0.09 μmol h^{-1}	—	211
MOF-FA1-W/TiO_2/Au	—	—	300–800 nm	CH_4	—	17.2 μmol g^{-1} h^{-1}	—	212
CdS/Ni-MOF	—	—	300 W lamp	CO	—	1.87 μmol g^{-1} h^{-1}	0.05%@365 nm	213
Co-MOF/Cu_2O	—	—	>420 nm	CO	~100%	3.83 μmol g^{-1} h^{-1}	—	214
TTCOF/NH_2-UiO-66(Zr)	—	—	≥420 nm	CO	98%	6.56 μmol g^{-1} h^{-1}	0.21%@420 nm	215
$ZnIn_2S_4$/MOF-808	—	—	Xe lamp	CO	—	8.21 μmol g^{-1} h^{-1}	—	216
CD@NH_2-UiO-66	—	Trolamine	>420 nm	CO	—	16.6 μmol g^{-1} h^{-1}	—	217
Co-MOF-3	$[Ru(bpy)_3]Cl_2$	Trolamine	≥400 nm	CO	100%	27.1 μmol g^{-1} h^{-1}	—	218
Pt@NH_2-UiO-66@Cu-TCPP	—	Triethylamine	>400 nm	CO	~100%	40.2 μmol g^{-1} h^{-1}	—	219
$Cs_3Bi_2Br_9$/MOF 525 Co	—	—	AM 1.5G	CO	99.50%	61.2 μmol g^{-1} h^{-1}	0.07%@420 nm	220
NH_2-UiO-66-Fc	—	Trolamine	400–780 nm	CO	100%	90.65 μmol g^{-1} h^{-1}	0.92%@350 nm	221
[Co2#@Cu-CAT]-$CsPbBr_3$ QDs	—	—	>400 nm	CO	—	133.4 μmol g^{-1} h^{-1}	—	222
Cu NWs@HKUST-1	—	—	>420 nm	CO	92%	176.2 μmol g^{-1} h^{-1}	—	223
[Emim]BF_4@PCN-250-Fe_2Co	—	—	>420 nm	CO	100%	313.3 μmol g^{-1} h^{-1}	2.9%@420 nm	224
Zr-MBA-Ru/Re-MOF	—	—	400–800 nm	CO	99%	440 μmol g^{-1} h^{-1}	0.11%@450 nm	225
In-MOF/GO	—	—	>420 nm	CO	100%	762.5 μmol g^{-1} h^{-1}	—	226
Co-MOL@GO	$[Ru(phen)_3](PF_6)_2$	Trolamine	=450 nm	CO	95%	18.0 mmol g^{-1} h^{-1}	—	107
PCN-250-Fe_2Mn	$[Ru(bpy)_3]Cl_2$	TIPA[c]	>420 nm	CO	82.17%	21.51 mmol g^{-1} h^{-1}	2.6%@450 nm	227
TiO_2/UiO-66	—	—	300 W lamp	CO	90.4%	1.9 μmol g^{-1} h^{-1}	—	228
				CH_4		17.9 μmol g^{-1} h^{-1}		
Zn-MOF/$BiVO_4$	—	—	>420 nm	CO	—	4.31 μmol g^{-1} h^{-1}	—	229
				CH_4		0.62 μmol g^{-1} h^{-1}		
Co-MOF/g-C_3N_4	—	—	>420 nm	CO	—	6.75 μmol g^{-1} h^{-1}	—	230
				CH_4		5.47 μmol g^{-1} h^{-1}		
$CsPbBr_3$/CuTCPP	—	—	300 W lamp	CO	—	11.8 μmol g^{-1} h^{-1}	0.05%@420 nm	231
				CH_4		2.95 μmol g^{-1} h^{-1}		
Ru/MOF-74/C_3N_4	—	—	300 W lamp	CO	—	11.8 μmol g^{-1} h^{-1}	7.8%@365 nm	232
				CH_4		7.3 μmol g^{-1} h^{-1}		
Cu-BTB-Fe	—	Lactic acid	350–780 nm	CO	69.24%	14.29 μmol g^{-1} h^{-1}	—	233
				CH_4		32.20 μmol g^{-1} h^{-1}		
NH_2-MIL-68@TP-TA	—	—	300 W lamp	CO	—	25 μmol g^{-1} h^{-1}	—	234
				CH_4		11.67 μmol g^{-1} h^{-1}		
Ag/NH_2-MIL-125(Ti) (T3-Ag)	—	Trolamine	AM 1.5G	CO	—	26.7 μmol g^{-1} h^{-1}	0.02%@450 nm	235
				CH_4	90.5%	63.3 μmol g^{-1} h^{-1}		
Au@PCN-222	—	—	≥420 nm	CO	—	29.1 μmol g^{-1} h^{-1}	0.24%@450 nm	34
				CH_4		2.5 μmol g^{-1} h^{-1}		
Ni@NTU-9/$BiVO_4$	—	—	300 W lamp	CO	99.20%	44.5 μmol g^{-1} h^{-1}	—	78
				CH_4		0.625 μmol g^{-1} h^{-1}		
Au-NC@MOF	—	CH_3OH	300–800 nm	CO	—	57.6 μmol g^{-1} h^{-1}	—	236
				CH_4		1.8 μmol g^{-1} h^{-1}		
g-C_3N_4-RGO-NH_2-MIL-125(Ti)	—	—	Visible light	CO	96.53%	95.9 μmol g^{-1} h^{-1}	0.41%@450 nm	237
				CH_4	3.47%	3.45 μmol g^{-1} h^{-1}		
Zr-PS3-FeTCPP$_{0.43}$	—	Triethylamine	500 W lamp	CO	54.64%	247.8 μmol g^{-1} h^{-1}	2.2%@360 nm	238
				CH_4	32.28%			
42%-TiO_2-in-MIL-101-Cr-NO_2	—	—	300 W lamp	CO	91%	11 mmol g^{-1} h^{-1}	11.3%@350 nm	75
				CH_4		1.1 mmol g^{-1} h^{-1}		
g-C_3N_4/M_a-M_bTCPP	—	Triethylamine	360–800 nm	CO	29%	12.3 μmol g^{-1} h^{-1}	—	239
				CH_4	27%	11.6 μmol g^{-1} h^{-1}		
				C_2H_6	44%	18.5 μmol g^{-1} h^{-1}		
Au@UiO-67-bpy-Cu	—	Trolamine	>400 nm	CH_3OH	96%	118.4 μmol g^{-1} h^{-1}	—	240
TiO_2@Cu-BTC-MOF	—	Triethylamine	W lamp	CH_3OH	—	4000 μmol g^{-1} h^{-1}	—	241
$(CsPbI_3)_{0.25}$ (4%Rh-a$_g$ZIF-62)$_{0.75}$	—	Trolamine	>400 nm	HCOOH	—	0.12 mM h^{-1}	—	111
NH_2-MIL-125(Ti)–Cu	—	Trolamine	>420 nm	HCOOH	—	30.1 μmol g^{-1} h^{-1}	1.18%@380 nm	242
Cu NCs@UiO-66-NH_2	—	Trolamine	250–385 nm	HCOOH	86%	128 μmol g^{-1} h^{-1}	—	243
PCN-222-Ni@UiO-67-NH_2	—	—	≥420 nm	HCOOH	73.2%	146 μmol g^{-1} h^{-1}	—	83
CA@PCN-222	—	Trolamine	400–800 nm	HCOO$^-$	—	280.4 μmol g^{-1} h^{-1}	—	244
$(PW_{12},Cp*Rh)$@UiO-67	$[Ru(bpy)_3]Cl_2$	Trolamine	>415 nm	HCOO$^-$	—	357.1 μmol g^{-1} h^{-1}	—	245
Cu_2O@POM_{12}@HKUST-4	—	BIH[d]	300 W lamp	HCOOH	100%	522.6 μmol g^{-1} h^{-1}	—	246
M68N@In-TCPP	—	—	Sunlight	HCOOH	85.4%	397.5 μmol g^{-1} h^{-1}	0.16%@400 nm	210
				CO		61.2 μmol g^{-1} h^{-1}		
Cu_2O@Cu-MOF/TiO_2	—	—	320–780 nm	CH_4	90%	366.0 μmol g^{-1} h^{-1}	—	247
				CO	4.5%	18.17 μmol g^{-1} h^{-1}		

Table 3 (Contd.)

Photocatalysts	Photosensitizers	SA^a	Light source	Products	Selectivity	Activity	AQE^b	Ref.
Zn$_2$GeO$_4$/ZIF-67	—	—	350 W lamp	C$_2$H$_6$	5.5%	22.71 μmol g^{-1} h^{-1}	0.913%@420 nm	248
				CH$_3$OH	31.27%	5.15 μmol g^{-1} h^{-1}		
				C$_2$H$_5$OH	24.73%	4.08 μmol g^{-1} h^{-1}		
Cu SAs/UiO-66-NH$_2$	—	Trolamine	>400 nm	CH$_3$OH	—	5.33 μmol g^{-1} h^{-1}	—	249
				C$_2$H$_5$OH		4.22 μmol g^{-1} h^{-1}		
g-C$_3$N$_4$/CuO@MIL-125(Ti)	—	—	300 W lamp	CO	3.4%	60.0 μmol g^{-1} h^{-1}	3.10%@420 nm	250
				CH$_3$OH	18.9%	332.4 μmol g^{-1} h^{-1}		
				CH$_3$CHO	20.3%	177.2 μmol g^{-1} h^{-1}		
				C$_2$H$_5$OH	57.4%	501.9 μmol g^{-1} h^{-1}		
Ce-UiO-66-bpydc-MOF	—	—	400–800 nm	CH$_3$COOH	99.50%	128 μmol g^{-1} h^{-1}	0.93%@450 nm	251

^{a} Sacrificial agents. ^{b} Apparent quantum efficiency. ^{c} Triisopropanolamine. ^{d} 2,3-Dihydro-1,3-dimethyl-2-phenyl-1H-benzimidazole.

MOFs through competitive linker nucleation with In nodes, forming coherent interfaces that enhanced structural stability and charge transfer. DFT calculations suggested that CO$_2$ molecules were favorable for adsorption at In–N sites of the In-TCPP shell, and H$_2$O molecules were preferably activated at the InO$_4$(OH)$_2$ sites of the M68N shell (Fig. 15a and b). The S-scheme mechanism promoted directed charge separation via built-in electric fields between the components, facilitating the spatial separation of charge carriers. Under concentrated sunlight, M68N@In-TCPP created an unparalleled yield of HCOOH (397.5 μmol g^{-1} h^{-1}) with a selectivity of 85.4%, which was higher than those of reported MOF-based photocatalysts. Notably, H$_2$O$_2$ (321.2 μmol g^{-1} h^{-1}) was also detected, achieving the utilization of photogenerated holes without photosensitizers, noble metals, or sacrificial agents. This work demonstrates a well-designed approach for solar-driven CO$_2$-to-chemical conversion, highlighting the potential of MOF composites in sustainable energy and carbon-neutral technology through reactant affinity engineering.

Karmakar et al. reported a visible-light-driven photocatalytic system with post-synthetic modified Ce-UiO-66-bpydc grafted with [Ru(bpy)$_2$Cl$_2$].[251] The obtained Ce-MOF-Ru^{II}-bpy promoted efficient metal-to-ligand charge transfer (MLCT) and leveraged the vacant low-lying 4f orbital of Ce^{IV} to facilitate rapid electron transport, as verified by TAS and X-ray structure absorption near edge spectroscopy (XANES). Under visible light (400–800 nm) irradiation, Ce-MOF-Ru^{II}-bpy achieved exceptional selectivity (99.5%) for double-carbon (C$_2$) product generation in aqueous media while suppressing the formation of C$_1$ and H$_2$ byproducts. Ce-MOF-Ru^{II}-bpy demonstrated a significantly enhanced activity with a CH$_3$COOH production rate of 128 μmol g^{-1} h^{-1}, representing a 7.4-fold improvement over Ce-MOF. In CO$_2$ adsorption measurements, the modified MOF achieved a saturation capacity of 37 cm^3 g^{-1}, which exceeded that of the pristine MOF by 1.9 times (Fig. 15c), indicating the significance of CO$_2$ adsorption capability in determining catalytic performance. According to DFT calculations, Ce^{III} was identified as the active site for CO$_2$ reduction. The in situ DRIFTS and Gibbs free energy analysis revealed the C–C coupling pathway for CH$_3$COOH synthesis. The synergistic effect of an appropriate photosensitizer, pore confinement of Ce-MOF, and unsaturated

Ce sites with a low-lying orbital contributed to the impressive high selectivity toward the C$_2$ product, which provides new insights into MOF composites in photocatalytic CO$_2$ reduction.

3.4 N$_2$ fixation

Nitrogen plays an indispensable role in modern agriculture and industry. Paradoxically, N$_2$, which constitutes 78% of the atmosphere, exists as a thermodynamically stable triple-bonded molecule. Therefore, chemically inert N$_2$ needs to be fixed and converted to NH$_3$ or other nitrogenous compounds.[252,253] Photocatalytic N$_2$ fixation is considered a promising strategy for N$_2$ fixation.[254] Recent advances demonstrate the emerging potential of MOF composites in photocatalytic N$_2$ fixation owing to their structural tunability and active site accessibility (Table 4).[255]

Ding et al. developed a Ru-anchored MOF-74/C$_3$N$_4$ composite via in situ synthesis (Fig. 16a).[232] With the dual validation of Nessler's agent and an ammonium ion composite electrode, a superior NH$_3$ yield of 8.1 mmol g^{-1} h^{-1} was detected over Ru/MOF-74/C$_3$N$_4$ under a 300 W Xe lamp, which is 3 times that of MOF-74/C$_3$N$_4$ and 6 times that of pure C$_3$N$_4$. The new energy level in the bandgap of MOF-74 introduced by Ru SAs and the type-II heterojunction mechanism inhibited electron–hole recombination while suppressing competing hydrogen evolution. DFT calculations demonstrated that Ru SAs can effectively decrease the energy barrier and Gibbs free energy
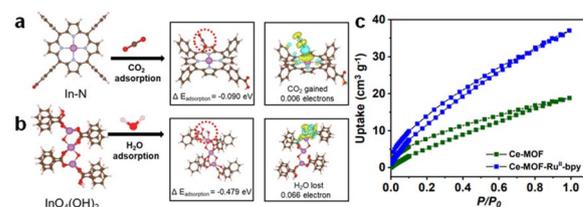

Fig. 15 DFT calculations of the charge difference density of (a) CO$_2$ adsorption at In–N sites and (b) H$_2$O adsorption at InO$_4$(OH)$_2$ sites. Magenta, red, light blue, brown, and pink spheres represent In, O, N, C, and H atoms, respectively.[210] Copyright 2025, Springer Nature. (c) CO$_2$ adsorption–desorption isotherms of Ce-MOF and Ce-MOF-Ru^{II}-bpy at 298 K.[251] Copyright 2023, Royal Society of Chemistry.

Table 4 MOF composites for photocatalytic N_2 fixation

Photocatalysts	SA[a]	Light source	Products	Activity	AQE[b]	Ref.
Nano-SH-MOF@H-C$_3$N$_4$	—	>420 nm	NH$_3$	0.12 µg mL^{-1} h^{-1}	0.12%@500 nm	256
Ru@MIL-125/MnO$_x$	—	>420 nm	NH$_3$	10.43 µmol g^{-1} h^{-1}	0.17%@500 nm	257
CeO$_2$/UNH(Ce)	—	250 W Hg light	NH$_3$	47.55 µmol L^{-1} h^{-1}	—	258
Pmo$_{10}$V$_2$@MIL-88A	Na$_2$SO$_3$	300 W Xe lamp	NH$_3$	50.82 µmol g^{-1} h^{-1}	0.29%@380 nm	259
Ru$_1$/d-UiO-66	—	300 W Xe lamp	NH$_3$	53.28 µmol g^{-1} h^{-1}	0.34%@300 nm	72
Ru/DUT-67(Zr)	—	300 W Xe lamp	NH$_3$	61.1 µmol g^{-1} h^{-1}	1.07%@280 nm	260
Ti$_3$C$_2$-QD/Ni-MOF	Na$_2$SO$_3$	300 W Xe lamp	NH$_3$	88.79 µmol g^{-1} h^{-1}	—	119
GSCe	—	=365 nm	NH$_3$	110.24 µmol L^{-1} h^{-1}	9.25%@365 nm	261
Au@PCN-221(Fe)	—	300 W Xe lamp	NH$_3$	129.2 µmol g^{-1} h^{-1}	0.33%@365 nm	262
UiO-66/PDA/CNNS	K$_2$SO$_3$	300 W Xe lamp	NH$_3$	147.8 µmol g^{-1} h^{-1}	0.86%@380 nm	263
Ru@Mo-MOF-tri	—	>400 nm	NH$_3$	637 µmol g^{-1} h^{-1}	—	264
Mo$_{72}$Fe$_{30}$@UiO-66	—	300 W Xe lamp	HNO$_3$	702.4 µg g^{-1} h^{-1}	0.072%@380 nm	265
MIL-125-NH$_2$@Co-HHTP	—	AM 1.5 G	NH$_3$	2.1 mmol g^{-1} h^{-1}	16.2%@365 nm	266
Ru/MOF-74/C$_3$N$_4$	CH$_3$OH	300 W Xe lamp	NH$_3$	8.1 mmol g^{-1} h^{-1}	—	232
Au@UiO-66/PTFE membranes	—	>400 nm	NH$_3$	18.9 mmol g^{-1} h^{-1}	1.54%@520 nm	32

[a] Sacrificial agents. [b] Apparent quantum efficiency.

in N_2 fixation. Pristine MOF-74 had no adsorption ability for N_2, which was consistent with the result that MOF-74 exhibited no obvious activity.

Apart from NH$_3$, NO$_3^-$ is also an important product in N_2 fixation. Li and coworkers designed a dual-active-site photocatalyst by integrating polyoxometalate (POM) Mo$_{72}$Fe$_{30}$ with UiO-66 for photocatalytic N_2 fixation under a 300 W Xe lamp (Fig. 16b).[265] The coordination microenvironment was modified

Fig. 16 (a) The synthesis process of a Ru-anchored MOF-74/C$_3$N$_4$ composite.[232] Copyright 2023, Elsevier. (b) Schematic illustration of the efficient storage and conversion of N_2 to HNO$_3$ by Mo$_{72}$Fe$_{30}$@UiO-66.[265] Copyright 2023, John Wiley and Sons.

to create unsaturated metal clusters with Lewis-acidic d-orbitals in UiO-66, promoting N_2 adsorption through $3\sigma_g$ orbital electron acceptance. The temperature-programmed desorption (TPD) characterization showed that Mo$_{72}$Fe$_{30}$@UiO-66 possessed one more desorption peak than UiO-66, indicating the better N_2 adsorption capacity of Mo$_{72}$Fe$_{30}$@UiO-66. Acting as electron sponges, Mo$_{72}$Fe$_{30}$ provided electrons to UiO-66, while holes accumulated on Mo$_{72}$Fe$_{30}$ for N_2 activation. According to the ion chromatograph results, the optimized HNO$_3$ yield of Mo$_{72}$Fe$_{30}$@UiO-66 was 702.4 µg g^{-1} h^{-1}, the better N_2 adsorption capacity of Mo$_{72}$Fe$_{30}$@UiO-66. Acting as an electron sponge, Mo$_{72}$Fe$_{30}$ provided electrons without sacrificial agent, 7 times and 24 times higher than that of UiO-66 and that of Mo$_{72}$Fe$_{30}$.

As demonstrated by the above two examples, the pivotal factor in photocatalytic N_2 fixation is N_2 adsorption, where MOFs exhibit exceptional advantage. Through rational structural engineering, the N_2 adsorption capacity of MOF composites can be precisely modulated, which effectively facilitates the subsequent catalytic process.

4. Conclusion and prospects

The rapid development of MOF composites for photocatalysis has gained significant momentum due to the unique flexibility and compatibility of MOFs. Integrating MOFs with other functional materials, such as metal NPs, semiconductors, and reticular materials, has transcended the limitations of pristine MOFs and further expanded the potential of MOF-based photocatalysts. These systems leverage synergistic effects that enhance light absorption, charge separation, and surface catalytic efficiency, effectively addressing some of the intrinsic limitations of pristine MOFs. Consequently, MOF composites have demonstrated performance across a variety of photocatalytic applications, including contaminant degradation, water splitting, CO$_2$ reduction, and N_2 fixation. The ability to engineer the electronic properties and catalytic sites within
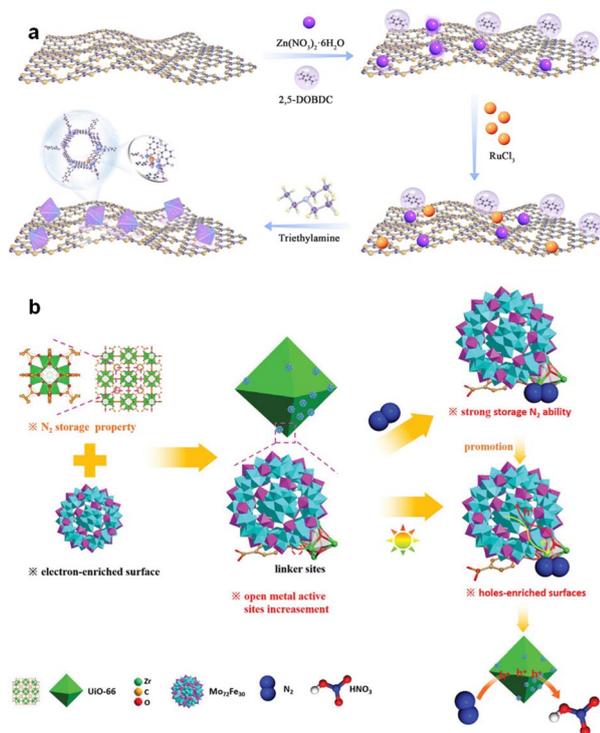
MOF composites allows for fine-tuning of the photocatalytic activity and selectivity.

Although MOF composites have demonstrated remarkable potential in photocatalysis, significant hurdles remain in translating these materials from laboratory research to practical applications. For metal/MOF composites, key challenges involve suppressing nanoparticle sintering and establishing robust metal–support interactions, as uncontrolled aggregation or residual surfactants can significantly compromise catalytic activity. Future research should focus on atomic-level precision synthesis to tailor the size, composition, and spatial distribution of metal clusters within MOFs, thereby enhancing metal–MOF coupling for improved performance.

The integration of semiconductors with MOFs often faces challenges such as rapid charge recombination and unfavorable band alignment. To address these issues, carefully engineered semiconductor/MOF heterojunctions (*e.g.*, type II, Z-scheme, or S-scheme) can significantly enhance charge separation and photocatalytic efficiency. Furthermore, selecting semiconductors with complementary electronic properties and precisely tuning their band structures, through linker functionalization or strategic doping, offers a promising strategy to suppress recombination losses while extending light absorption across a broader spectral range.

One major challenge in developing reticular material/MOF composites has been the difficulty of establishing strong covalent bonding between COFs and MOFs at their interfaces, primarily due to distinct chemical natures. This limitation results in weak interfacial connections that significantly hinder efficient charge-carrier transfer and separation. A key solution is post-synthetic functionalization of the MOF or COF to introduce complementary reactive groups that form covalent linkages. Similar strategies include growing a COF directly on the MOF surface or using layer-by-layer assembly to create intimate, well-anchored interfaces. Looking ahead, atomic-level assembly of two-dimensional MOF and COF layers (2D/2D heterostructures) is a promising frontier-precisely stacking MOF nanosheets with COF sheets to engineer the interface on the atomic scale.

Other material/MOF composites offer unique opportunities but also present distinct challenges that demand customized solutions. For UCNPs/MOF systems, the primary limitation stems from the low quantum yield of UCNPs, severely constraining their near-infrared light utilization efficiency. Moreover, several critical issues hinder the photocatalytic performance of various MOF-based composites: the poor electronic conductivity of metal oxide/MOF systems, the intricate synthesis procedures required for metal phosphide/MOF hybrids, the limited thermal stability of metal sulfide/MOF composites, and the inadequate cycling durability of carbon material/MOF photocatalysts. Developing cost-effective strategies to integrate emerging functional materials (*e.g.*, MXenes, COFs, and 2D materials) with MOFs represents a promising direction for future research in this field.

In addition to the aforementioned potential approaches for achieving each of the strategies, innovative strategies are needed to unlock the full potential of MOF composites in photocatalysis.

4.1 Structural control and precise design

Presently, the combination of MOFs and other components into composites, in many cases, lacks elaborate structural control.[267] Fabrication of MOF composites at molecular and even atomic scales, such as precise location control of the guest species,[268] would be significant not only for fundamental structure–property understanding but also for optimized photocatalytic performance. Future advancements in this field can focus on atomic-level positioning of active sites. Developing synthetic strategies to precisely anchor catalytic species (*e.g.*, single atoms, clusters, or co-catalysts) at specific locations within MOFs (*e.g.*, nodes, linkers, or pore cavities) could enhance charge transfer and active-site accessibility. For hierarchical structuring of MOF composites, beyond simple hybridization, future designs should consider multi-scale structural engineering, including controlled spatial distribution of components (*e.g.*, core–shell, Janus, or spatially graded architectures) to optimize light absorption, charge separation, and reactant diffusion.

4.2 Exploring the roles of the components

As the structure–function relationships of MOF composites grow increasingly complex, exploring the interplay between various factors influencing their performance is crucial for designing enhanced MOF-based photocatalysts. Distinct from traditional inorganic semiconductors, the well-defined structures of MOFs offer significant advantages in precisely unveiling the photocatalytic mechanism. In previous reports, a series of standardized characterization techniques have been employed to comprehensively evaluate the properties of MOF composites, such as powder X-ray diffraction for crystallographic structure determination, electron microscopy for morphological characterization, N_2 adsorption–desorption analysis for porosity and specific surface area evaluation, diffuse reflectance ultraviolet-visible spectroscopy for light absorption range measurement, X-ray photoelectron spectroscopy for surface elemental composition and electronic transfer analysis, and photoluminescence spectroscopy for charge carrier separation efficiency assessment. The multi-technique approach ensures fundamental understanding of the structural and functional characteristics of MOF composites. Moreover, with theoretical calculations[269] and advanced characterization techniques such as TAS,[200] XAS,[270] KPFM,[218] and *in situ* DRIFTS,[226] MOF composites can be accurately characterized, encompassing quantifying interfacial stresses in interface interactions and accurate tracing of electron flow to clarify the charge transfer mechanisms in MOF composites. This deeper insight into their structural and functional intricacies will lead to more foundational understanding of photocatalytic processes.

4.3 Microenvironment modulation around catalytic sites

Thanks to the atomically precise tunability of MOF structures and inspired by enzymatic catalysis, MOFs offer an ideal platform for microenvironment modulation around catalytic centers,[271] which presents a significant opportunity to enhance

photocatalytic performance. However, current investigations into this topic are still limited and need to be strengthened. Future studies should focus on developing advanced synthetic strategies to systematically modify SBUs and organic linkers to create tailored microenvironments, such as confined hydrophobic pockets or charged domains, favoring specific photocatalytic reactions. Machine learning and DFT calculations are utilized to predict optimal microenvironment configurations for specific reactions, accelerating the discovery of high-performance MOF photocatalysts.

4.4 Developing MOF composites for tandem photocatalytic reactions

Achieving high selectivity and catalytic efficiency in photocatalytic reactions remains a significant challenge, particularly in complex, multi-step processes.[272] MOF composites, integrating multiple functional components can mimic natural enzymatic systems where cascade reactions occur in a confined environment. By precisely controlling the spatial distribution and electronic interactions between different active sites, these composites could enable synergistic effects, such as enhanced charge separation, substrate channeling, and intermediate stabilization. The development of multi-component MOF composites,[273] where different active sites work in concert to catalyze sequential reactions, can further improve catalytic efficiency and expand the scope of possible reactions.

4.5 Enhancing stability

Although MOF composites for photocatalysis hold immense promise, their stability during catalytic reactions is a major concern.[274] The degradation of MOF structures under prolonged light irradiation, in harsh chemical environments, or under thermal fluctuations can significantly reduce their photocatalytic efficiency and recyclability. Moreover, the decomposition of MOF composites may generate potential false positive catalytic results.[22] Although isotopic labeling can be used to identify product sources, it has limitations such as incomplete detection of molecular ion signatures, discrepancies between ion flow and molecular ion peak intensities, and inconsistent proportionality between ^{13}C and ^{16}O isotopic fragments. To address this challenge, future research should focus on multiple strategies to enhance the robustness of MOF composites: incorporating protective coatings (*e.g.*, carbon layers, polymers, or inorganic shells) can shield MOFs from degradation while maintaining photocatalytic activity; developing dynamic MOF composites capable of self-repairing minor structural damage (*e.g.*, *via* reversible ligand exchange or guest-induced healing) could extend their operational lifespan. Additionally, many MOF-based photocatalysts rely on sacrificial agents (*e.g.*, triethanolamine and triethylamine) to enhance charge separation, but these additives may accelerate MOF decomposition. To address this limitation, overall redox photocatalysis has emerged as a promising strategy, in which reduction and oxidation reactions are coupled within a single system, increasing the durability of the catalyst and the economic value by avoiding the use of sacrificial agents.[275,276]

4.6 Scalable and sustainable synthesis

While significant progress has been made in synthesizing MOF composites to promote photocatalytic performance, many of the methods developed are not easily scalable or cost-effective for large-scale production.[277] Conventional solvothermal synthesis often requires prolonged reaction times, high energy consumption, and large quantities of organic solvents, which raises economic and ecological concerns. To address these limitations, techniques such as microwave-assisted synthesis, continuous flow production, electrochemical routes, and mechanochemical methods can be optimized for the scalable production of MOF composites.[278,279] By advancing these scalable synthesis techniques, the field can move toward economically viable and environmentally friendly production of MOF composites, unlocking their full potential for real-world photocatalytic applications.

4.7 Exploring novel MOF composites

The discovery and exploration of new MOF composites, particularly those with unique structures or properties, can open up new avenues for photocatalysis. In this regard, large language models (LLMs),[280,281] machine learning (ML),[282] artificial intelligence (AI),[283] and high-throughput screening protocols[284] can accelerate the development of novel MOFs with desirable photocatalytic properties. Additionally, exploring unconventional MOF structures, such as those with mixed-metal nodes,[285] flexible frameworks,[286] or hierarchical porosity,[287] can lead to the development of materials with unprecedented photocatalytic performance. Mixed-metal nodes may introduce synergistic electronic effects, improving charge carrier dynamics, while flexible MOFs could enable adaptive guest interactions for enhanced substrate activation. Hierarchical porosity, combining micro- and mesopores, can facilitate mass transport and expose more active sites, crucial for large-molecule photocatalytic reactions.

More than that, a persistent challenge in MOF-based photocatalysis research lies in the prevalence of conceptual ambiguities and oversimplified mechanistic interpretations, frequently arising from inadequate experimental evidence and incomplete mechanistic understanding. To establish reliable structure–activity relationships, comprehensive characterization of MOF composites must employ advanced spectroscopic methods. Essential spectroscopic tools include *in situ* DRIFTS for monitoring surface-bound intermediates, EPR spectroscopy for identifying radical species and paramagnetic centers, and time-resolved photoluminescence (TRPL) for quantifying excited-state lifetimes and charge-carrier dynamics. These techniques, particularly when complemented by transient absorption spectroscopy, offer direct insights into charge-transfer mechanisms and trap-state distributions that govern photocatalytic activity. Moreover, to prevent mechanistic oversimplification, we strongly recommend correlating observations from multiple orthogonal techniques, including EPR, *in situ* DRIFTS, and UV-vis spectroscopy, with theoretical band-structure calculations. Such a multimodal approach provides more reliable evidence than performance enhancement alone for identifying active species. Particularly crucial are *in situ* and *operando* measurements under actual

catalytic conditions, which enable direct correlation between observed intermediates and functional behaviour.

In summary, the journey towards optimizing MOF composites for photocatalysis is a multifaceted endeavor, requiring collaboration across chemistry, materials science, and engineering. With continued innovation in material design, mechanistic insights, and scalable fabrication, MOF composites are poised to revolutionize photocatalysis, contributing to sustainable energy solutions and environmental remediation. The future promises an era where MOF composites shine even brighter in photocatalysis.

Data availability

No primary research results, software, or code have been included, and no new data were generated or analyzed as part of this review.

Author contributions

Chenxi Zhang: conceptualization, funding acquisition, visualization, writing – original draft, writing – review & editing. Yanhong Wu: investigation, visualization, writing – review & editing. Dandan Li: conceptualization, funding acquisition, writing – review & editing. Hai-Long Jiang: conceptualization, funding acquisition, project administration, supervision, writing – review & editing.

Conflicts of interest

There are no conflicts to declare.

Acknowledgements

References

1 J. Gong, C. Li and M. R. Wasielewski, *Chem. Soc. Rev.*, 2019, **48**, 1862–1864.

2 A. Wagner, C. D. Sahm and E. Reisner, *Nat. Catal.*, 2020, **3**, 775–786.

3 Z. Wang, T. Hisatomi, R. Li, K. Sayama, G. Liu, K. Domen, C. Li and L. Wang, *Joule*, 2021, **5**, 344–359.

4 K. Sun, Y. Huang, F. Sun, Q. Wang, Y. Zhou, J. Wang, Q. Zhang, X. Zheng, F. Fan, Y. Luo, J. Jiang and H.-L. Jiang, *Nat. Chem.*, 2024, **16**, 1638–1646.

5 S. E. Braslavsky, A. M. Braun, A. E. Cassano, A. V. Emeline, M. I. Litter, L. Palmisano, V. N. Parmon and N. Serpone, *Pure Appl. Chem.*, 2011, **83**, 931–1014.

6 R. Su, Y. Zhu, B. Gao and Q. Li, *Water Res.*, 2024, **251**, 121119.

7 S. Thakur, A. Ojha, S. K. Kansal, N. K. Gupta, H. C. Swart, J. Cho, A. Kuznetsov, S. Sun and J. Prakash, *Adv. Powder Mater.*, 2024, **3**, 100233.

8 F. Wang and H. Duan, *Chem Catal.*, 2022, **2**, 644–646.

9 H. Jiao, C. Wang, L. Xiong and J. Tang, *Acc. Mater. Res.*, 2022, **3**, 1206–1219.

10 H.-G. Jin, P.-C. Zhao, Y. Qian, J.-D. Xiao, Z.-S. Chao and H.-L. Jiang, *Chem. Soc. Rev.*, 2024, **53**, 9378–9418.

11 Q. Wang and K. Domen, *Chem. Rev.*, 2020, **120**, 919–985.

12 C. Xu, P. Ravi Anusuyadevi, C. Aymonier, R. Luque and S. Marre, *Chem. Soc. Rev.*, 2019, **48**, 3868–3902.

13 A. Meng, L. Zhang, B. Cheng and J. Yu, *Adv. Mater.*, 2019, **31**, 1807660.

14 J. Shi, J. Zhang, L. Yang, M. Qu, D.-C. Qi and K. H. L. Zhang, *Adv. Mater.*, 2021, **33**, 2006230.

15 H. Furukawa, K. E. Cordova, M. O'Keeffe and O. M. Yaghi, *Science*, 2013, **341**, 1230444.

16 H.-C. J. Zhou and S. Kitagawa, *Chem. Soc. Rev.*, 2014, **43**, 5415–5418.

17 G. Cai, P. Yan, L. Zhang, H.-C. Zhou and H.-L. Jiang, *Chem. Rev.*, 2021, **121**, 12278–12326.

18 R.-J. Wei, P.-Y. You, H. Duan, M. Xie, R.-Q. Xia, X. Chen, X. Zhao, G.-H. Ning, A. I. Cooper and D. Li, *J. Am. Chem. Soc.*, 2022, **144**, 17487–17495.

19 B.-T. Liu, S.-H. Gong, X.-T. Jiang, Y. Zhang, R. Wang, Z. Chen, S. Zhang, K. O. Kirlikovali, T.-F. Liu, O. K. Farha and R. Cao, *Nat. Synth.*, 2023, **2**, 873–879.

20 W. Gong, X. Chen, M. Wahiduzzaman, H. Xie, K. O. Kirlikovali, J. Dong, G. Maurin, O. K. Farha and Y. Cui, *J. Am. Chem. Soc.*, 2024, **146**, 2141–2150.

21 J.-D. Xiao and H.-L. Jiang, *Acc. Chem. Res.*, 2019, **52**, 356–366.

22 K. Sun, Y. Qian and H.-L. Jiang, *Angew. Chem., Int. Ed.*, 2023, **62**, e202217565.

23 W. Wang, D. Chen, F. Li, X. Xiao and Q. Xu, *Chem*, 2024, **10**, 86–133.

24 A. Dhakshinamoorthy, Z. Li, S. Yang and H. Garcia, *Chem. Soc. Rev.*, 2024, **53**, 3002–3035.

25 J. Guo, Y. Wan, Y. Zhu, M. Zhao and Z. Tang, *Nano Res.*, 2021, **14**, 2037–2052.

26 Y. Qian, F. Zhang and H. Pang, *Adv. Funct. Mater.*, 2021, **31**, 2104231.

27 D. Chen, Y.-T. Zheng, N.-Y. Huang and Q. Xu, *EnergyChem*, 2024, **6**, 100115.

28 A. Hayat, S. Rauf, B. Al Alwan, A. El Jery, N. Almuqati, S. Melhi, M. A. Amin, Y. Al-Hadeethi, M. Sohail, Y. Orooji and W. Lv, *Mater. Today Energy*, 2024, **41**, 101542.

29 Q. Yang, Q. Xu and H.-L. Jiang, *Chem. Soc. Rev.*, 2017, **46**, 4774–4808.

30 S. Li, P. Miao, Y. Zhang, J. Wu, B. Zhang, Y. Du, X. Han, J. Sun and P. Xu, *Adv. Mater.*, 2021, **33**, 2000086.

31 B. Zhang, X. Cao, J. Wen, S. Guo, X. Duan and X.-M. Zhang, *Coord. Chem. Rev.*, 2024, **518**, 216113.

32 L.-W. Chen, Y.-C. Hao, Y. Guo, Q. Zhang, J. Li, W.-Y. Gao, L. Ren, X. Su, L. Hu, N. Zhang, S. Li, X. Feng, L. Gu,

Y.-W. Zhang, A.-X. Yin and B. Wang, *J. Am. Chem. Soc.*, 2021, **143**, 5727–5736.

33 Q.-Q. Huang, Z.-B. Fang, K. Pang, W.-K. Qin, T.-F. Liu and R. Cao, *Adv. Funct. Mater.*, 2022, **32**, 2205147.

34 T. Huang, J. Han, Z. Li, Y. Hong, X. Gu, Y. Wu, Y. Zhang and S. Liu, *Angew. Chem., Int. Ed.*, 2025, **64**, e202500269.

35 K. M. Choi, D. Kim, B. Rungtaweevoranit, C. A. Trickett, J. T. D. Barmanbek, A. S. Alshammari, P. Yang and O. M. Yaghi, *J. Am. Chem. Soc.*, 2017, **139**, 356–362.

36 Q. Liu, C. Zeng, L. Ai, Z. Hao and J. Jiang, *Appl. Catal., B*, 2018, **224**, 38–45.

37 L. Xiao, Q. Zhang, P. Chen, L. Chen, F. Ding, J. Tang, Y.-J. Li, C.-T. Au and S.-F. Yin, *Appl. Catal., B*, 2019, **248**, 380–387.

38 M. Sayed, J. Yu, G. Liu and M. Jaroniec, *Chem. Rev.*, 2022, **122**, 10484–10537.

39 Y. Zhang, F. Ma, M. Ling, H. Zheng, Y. Wu and L. Li, *Chem. Eng. J.*, 2023, **464**, 142762.

40 H. Wang, L. Zhang, Z. Chen, J. Hu, S. Li, Z. Wang, J. Liu and X. Wang, *Chem. Soc. Rev.*, 2014, **43**, 5234–5244.

41 S. Bai, J. Jiang, Q. Zhang and Y. Xiong, *Chem. Soc. Rev.*, 2015, **44**, 2893–2939.

42 Y.-Z. Chen, Z. U. Wang, H. Wang, J. Lu, S.-H. Yu and H.-L. Jiang, *J. Am. Chem. Soc.*, 2017, **139**, 2035–2044.

43 P. Kumari, N. Bahadur, L. Kong, L. A. O'Dell, A. Merenda and L. F. Dumée, *Mater. Adv.*, 2022, **3**, 2309–2323.

44 J.-D. Xiao, Q. Shang, Y. Xiong, Q. Zhang, Y. Luo, S.-H. Yu and H.-L. Jiang, *Angew. Chem., Int. Ed.*, 2016, **55**, 9389–9393.

45 J.-D. Xiao, L. Han, J. Luo, S.-H. Yu and H.-L. Jiang, *Angew. Chem., Int. Ed.*, 2018, **57**, 1103–1107.

46 Y. Pan, Y. Qian, X. Zheng, S.-Q. Chu, Y. Yang, C. Ding, X. Wang, S.-H. Yu and H.-L. Jiang, *Natl. Sci. Rev.*, 2021, **8**, nwaa224.

47 Z.-X. Sun, K. Sun, M.-L. Gao, Ö. Metin and H.-L. Jiang, *Angew. Chem., Int. Ed.*, 2022, **61**, e202206108.

48 Y. Wang, W. Zhang, D. Li, J. Guo, Y. Yu, K. Ding, W. Duan, X. Li, H. Liu, P. Su, B. Liu and J. Li, *Adv. Sci.*, 2021, **8**, 2004456.

49 W. Zhang, A. R. Mohamed and W.-J. Ong, *Angew. Chem., Int. Ed.*, 2020, **59**, 22894–22915.

50 J. Abdul Nasir, A. Munir, N. Ahmad, T. u. Haq, Z. Khan and Z. Rehman, *Adv. Mater.*, 2021, **33**, 2105195.

51 G. Liao, C. Li, S.-Y. Liu, B. Fang and H. Yang, *Trends Chem.*, 2022, **4**, 111–127.

52 S. Chen, C. Li, K. Domen and F. Zhang, *Joule*, 2023, **7**, 2445–2467.

53 Q. Xu, L. Zhang, J. Yu, S. Wageh, A. A. Al-Ghamdi and M. Jaroniec, *Mater. Today*, 2018, **21**, 1042–1063.

54 H. Wang, X. Zhang, W. Zhang, M. Zhou and H.-L. Jiang, *Angew. Chem., Int. Ed.*, 2024, **63**, e202401443.

55 J. Yang, D. Wang, H. Han and C. Li, *Acc. Chem. Res.*, 2013, **46**, 1900–1909.

56 B. Qiu, M. Du, Y. Ma, Q. Zhu, M. Xing and J. Zhang, *Energy Environ. Sci.*, 2021, **14**, 5260–5288.

57 W. Gao, H. Li, J. Hu, Y. Yang, Y. Xiong, J. Ye, Z. Zou and Y. Zhou, *Chem. Sci.*, 2024, **15**, 14081–14103.

58 Z. Li, J.-D. Xiao and H.-L. Jiang, *ACS Catal.*, 2016, **6**, 5359–5365.

59 X. Ma, L. Wang, Q. Zhang and H.-L. Jiang, *Angew. Chem., Int. Ed.*, 2019, **58**, 12175–12179.

60 J. Zhang, T. Bai, H. Huang, M.-H. Yu, X. Fan, Z. Chang and X.-H. Bu, *Adv. Mater.*, 2020, **32**, 2004747.

61 M. Xu, D. Li, K. Sun, L. Jiao, C. Xie, C. Ding and H.-L. Jiang, *Angew. Chem., Int. Ed.*, 2021, **60**, 16372–16376.

62 X. Huang, X. Li, Q. Luan, K. Zhang, Z. Wu, B. Li, Z. Xi, W. Dong and G. Wang, *Nano Res.*, 2021, **14**, 4250–4257.

63 Y.-N. Gong, J.-H. Mei, J.-W. Liu, H.-H. Huang, J.-H. Zhang, X. Li, D.-C. Zhong and T.-B. Lu, *Appl. Catal., B*, 2021, **292**, 120156.

64 S. Wang, K. Gao, Y. Cui, S. Li, H. Zhang, B. Zhang, J. Wu, H. Hou and S. Zang, *Nano Res.*, 2023, **16**, 4715–4722.

65 Y. Wang, B. Niu, Z. Zhang, J. Li, H. Sheng, W. Xu, J. Cheng, Z. Hao, D. Duan and J. Li, *Nano Lett.*, 2024, **24**, 12628–12633.

66 L. Yuan, P. Du, C. Zhang, Y. Xi, Y. Zou, J. Li, Y. Bi, T. Bao, C. Liu and C. Yu, *Appl. Catal., B*, 2025, **364**, 124855.

67 Z.-H. Xue, D. Luan, H. Zhang and X. W. Lou, *Joule*, 2022, **6**, 92–133.

68 H. Liu, M. Cheng, Y. Liu, J. Wang, G. Zhang, L. Li, L. Du, G. Wang, S. Yang and X. Wang, *Energy Environ. Sci.*, 2022, **15**, 3722–3749.

69 P. Zhou, M. Luo and S. Guo, *Nat. Rev. Chem.*, 2022, **6**, 823–838.

70 K. Kong, H. Zhang, A. Han, F. Li and D. Wang, *Energy Environ. Sci.*, 2024, **17**, 7649–7680.

71 S.-M. Wu and P. Schmuki, *Adv. Mater.*, 2025, **37**, 2414889.

72 G. Ren, J. Zhao, Z. Zhao, Z. Li, L. Wang, Z. Zhang, C. Li and X. Meng, *Angew. Chem., Int. Ed.*, 2024, **63**, e202314408.

73 Y. Pan, D. Li and H.-L. Jiang, *Chem.–Eur. J.*, 2018, **24**, 18403–18407.

74 H.-Q. Xu, S. Yang, X. Ma, J. Huang and H.-L. Jiang, *ACS Catal.*, 2018, **8**, 11615–11621.

75 Z. Jiang, X. Xu, Y. Ma, H. S. Cho, D. Ding, C. Wang, J. Wu, P. Oleynikov, M. Jia, J. Cheng, Y. Zhou, O. Terasaki, T. Peng, L. Zan and H. Deng, *Nature*, 2020, **586**, 549–554.

76 W. Xu, J. Wang, H. Yu, P. Liu, G.-R. Zhang, H. Huang and D. Mei, *Appl. Catal., B*, 2022, **308**, 121218.

77 Z.-F. Lin, T.-H. Wang, P. Venkatesan and R.-A. Doong, *Chem. Eng. J.*, 2025, **505**, 159411.

78 L. Zhao, J. Bian, X. Zhang, L. Bai, L. Xu, Y. Qu, Z. Li, Y. Li and L. Jing, *Adv. Mater.*, 2022, **34**, 2205303.

79 K. Sun, Y. Qian, D. Li and H.-L. Jiang, *Adv. Mater.*, 2024, 2411118.

80 C. Liu, L. Lin, Q. Sun, J. Wang, R. Huang, W. Chen, S. Li, J. Wan, J. Zou and C. Yu, *Chem. Sci.*, 2020, **11**, 3680–3686.

81 Y. Li, L. Liu, T. Meng, L. Wang and Z. Xie, *ACS Nano*, 2023, **17**, 2932–2942.

82 S. Wang, Z. Ai, X. Niu, W. Yang, R. Kang, Z. Lin, A. Waseem, L. Jiao and H.-L. Jiang, *Adv. Mater.*, 2023, **35**, 2302512.

83 H.-B. Huang, Z.-B. Fang, R. Wang, L. Li, M. Khanpour, T.-F. Liu and R. Cao, *Small*, 2022, **18**, 2200407.

84 X. Chu, S. Liu, B.-B. Luan, Y. Zhang, Y. Xi, L.-H. Shao, F.-M. Zhang and Y.-Q. Lan, *Angew. Chem., Int. Ed.*, 2025, **64**, e202422940.

85 X. Chen, X. Zhang and Y. Zhao, *Chem. Soc. Rev.*, 2025, **54**, 152–177.

86 X. Li, H. Wu, S. Yin, C. Yu, Y. Shao, D. Zhou and P. She, *Chem. Synth.*, 2025, **5**, 29.

87 D. Li, S.-H. Yu and H.-L. Jiang, *Adv. Mater.*, 2018, **30**, 1707377.

88 M. Li, Z. Zheng, Y. Zheng, C. Cui, C. Li and Z. Li, *ACS Appl. Mater. Interfaces*, 2017, **9**, 2899–2905.

89 M. Li, J. Wang, Y. Zheng, Z. Zheng, C. Li and Z. Li, *Inorg. Chem. Front.*, 2017, **4**, 1757–1764.

90 H. Zhang, W. Zhang, S. Gao, X. Lu, D. Zhang, X. Zhang and M. Wang, *Appl. Phys. A*, 2022, **128**, 499.

91 H. Ren, R. Bai, F. Huang, J. Zhang and L. Wang, *Cryst. Growth Des.*, 2022, **22**, 4864–4873.

92 S. J. Shah, W. Li, Y. Tang, Y. Hu, S. Jiang, H. He, R. Wang, Z. Zhao and Z. Zhao, *Appl. Catal., B*, 2022, **315**, 121555.

93 C. Zhang, C. Xie, Y. Gao, X. Tao, C. Ding, F. Fan and H.-L. Jiang, *Angew. Chem., Int. Ed.*, 2022, **61**, e202204108.

94 A. Ray, S. Sultana, L. Paramanik and K. M. Parida, *J. Mater. Chem. A*, 2020, **8**, 19196–19245.

95 L.-f. Hong, R.-t. Guo, Y. Yuan, X.-y. Ji, Z.-d. Lin, Z.-s. Li and W.-g. Pan, *ChemSusChem*, 2021, **14**, 539–557.

96 Y. Yang, C. Zhou, W. Wang, W. Xiong, G. Zeng, D. Huang, C. Zhang, B. Song, W. Xue, X. Li, Z. Wang, D. He, H. Luo and Z. Ouyang, *Chem. Eng. J.*, 2021, **405**, 126547.

97 C. Li, D. Zhu, S. Cheng, Y. Zuo, Y. Wang, C. Ma and H. Dong, *Chin. Chem. Lett.*, 2022, **33**, 1141–1153.

98 K. Sun, M. Liu, J. Pei, D. Li, C. Ding, K. Wu and H.-L. Jiang, *Angew. Chem., Int. Ed.*, 2020, **59**, 22749–22755.

99 S. Kampouri, T. N. Nguyen, C. P. Ireland, B. Valizadeh, F. M. Ebrahim, G. Capano, D. Ongari, A. Mace, N. Guijarro, K. Sivula, A. Sienkiewicz, L. Forró, B. Smit and K. C. Stylianou, *J. Mater. Chem. A*, 2018, **6**, 2476–2481.

100 L. Wu, Y. Tong, L. Gu, Z. Xue and Y. Yuan, *Sustainable Energy Fuels*, 2018, **2**, 2502–2506.

101 Y. Zhang and Z. Jin, *Phys. Chem. Chem. Phys.*, 2019, **21**, 8326–8341.

102 S. Cao and J. Yu, *J. Photochem. Photobiol., C*, 2016, **27**, 72–99.

103 Y. Xu, S. Li, M. Chen, J. Zhang and F. Rosei, *Trends Chem.*, 2022, **4**, 984–1004.

104 M. Samy, M. G. Ibrahim, M. Fujii, K. E. Diab, M. ElKady and M. Gar Alalm, *Chem. Eng. J.*, 2021, **406**, 127152.

105 L. Liu, H. Meng, Y. Chai, X. Chen, J. Xu, X. Liu, W. Liu, D. M. Guldi and Y. Zhu, *Angew. Chem., Int. Ed.*, 2023, **62**, e202217897.

106 X. Zhou, T. Wang, D. He, P. Chen, H. Liu, H. Lv, H. Wu, D. Su, H. Pang and C. Wang, *Angew. Chem., Int. Ed.*, 2024, **63**, e202408989.

107 J.-W. Wang, L.-Z. Qiao, H.-D. Nie, H.-H. Huang, Y. Li, S. Yao, M. Liu, Z.-M. Zhang, Z.-H. Kang and T.-B. Lu, *Nat. Commun.*, 2021, **12**, 813.

108 J. Hou, Z. Wang, P. Chen, V. Chen, A. K. Cheetham and L. Wang, *Angew. Chem., Int. Ed.*, 2020, **59**, 19434–19449.

109 Z.-C. Kong, J.-F. Liao, Y.-J. Dong, Y.-F. Xu, H.-Y. Chen, D.-B. Kuang and C.-Y. Su, *ACS Energy Lett.*, 2018, **3**, 2656–2662.

110 L.-Y. Wu, Y.-F. Mu, X.-X. Guo, W. Zhang, Z.-M. Zhang, M. Zhang and T.-B. Lu, *Angew. Chem., Int. Ed.*, 2019, **58**, 9491–9495.

111 W. Huang, B. Chan, Y. Yang, P. Chen, J. Wang, L. Casey, C. Atzori, T. Schulli, O. Mathon, H. G. Hackbarth, N. M. Bedford, D. Appadoo, X. Li, T. Lin, R. Lin, J. Lee, Z. Wang, V. Chen, A. K. Cheetham, L. Wang and J. Hou, *J. Am. Chem. Soc.*, 2025, **147**, 3195–3205.

112 A. VahidMohammadi, J. Rosen and Y. Gogotsi, *Science*, 2021, **372**, eabf1581.

113 X. Li, Z. Huang, C. E. Shuck, G. Liang, Y. Gogotsi and C. Zhi, *Nat. Rev. Chem.*, 2022, **6**, 389–404.

114 K. R. G. Lim, M. Shekhirev, B. C. Wyatt, B. Anasori, Y. Gogotsi and Z. W. Seh, *Nat. Synth.*, 2022, **1**, 601–614.

115 X. Zhuang, S. Zhang, Y. Tang, F. Yu, Z. Li and H. Pang, *Coord. Chem. Rev.*, 2023, **490**, 215208.

116 Y. Li, Y. Liu, Z. Wang, P. Wang, Z. Zheng, H. Cheng, Y. Dai and B. Huang, *Chem. Eng. J.*, 2021, **411**, 128446.

117 L. Shi, C. Wu, Y. Wang, Y. Dou, D. Yuan, H. Li, H. Huang, Y. Zhang, I. D. Gates, X. Sun and T. Ma, *Adv. Funct. Mater.*, 2022, **32**, 2202571.

118 Z. Ajmal, A. Hayat, A. Qadeer, Y. Zhao, E. H. Ibrahim, M. u. Haq, K. Iqbal, M. Imran, M. Kuku, I. Hussain, H. Ali, Y. Orooji, J. L. Zhou and T. Ben, *Coord. Chem. Rev.*, 2025, **523**, 216226.

119 J. Qin, B. Liu, K.-H. Lam, S. Song, X. Li and X. Hu, *ACS Sustainable Chem. Eng.*, 2020, **8**, 17791–17799.

120 R. Das, C. D. Vecitis, A. Schulze, B. Cao, A. F. Ismail, X. Lu, J. Chen and S. Ramakrishna, *Chem. Soc. Rev.*, 2017, **46**, 6946–7020.

121 S. Bolisetty, M. Peydayesh and R. Mezzenga, *Chem. Soc. Rev.*, 2019, **48**, 463–487.

122 K. N. Heck, S. Garcia-Segura, P. Westerhoff and M. S. Wong, *Acc. Chem. Res.*, 2019, **52**, 906–915.

123 V. I. Parvulescu, F. Epron, H. Garcia and P. Granger, *Chem. Rev.*, 2022, **122**, 2981–3121.

124 H. Anwer, A. Mahmood, J. Lee, K.-H. Kim, J.-W. Park and A. C. K. Yip, *Nano Res.*, 2019, **12**, 955–972.

125 L. N. Pincus, A. W. Lounsbury and J. B. Zimmerman, *Acc. Chem. Res.*, 2019, **52**, 1206–1214.

126 J. Chakraborty, I. Nath and F. Verpoort, *Chem. Soc. Rev.*, 2022, **51**, 1124–1138.

127 B. Weng, M. Zhang, Y. Lin, J. Yang, J. Lv, N. Han, J. Xie, H. Jia, B.-L. Su, M. Roeffaers, J. Hofkens, Y. Zhu, S. Wang, W. Choi and Y.-M. Zheng, *Nat. Rev. Clean Technol.*, 2025, **1**, 201–215.

128 S. Rojas and P. Horcajada, *Chem. Rev.*, 2020, **120**, 8378–8415.

129 X. Zhao, J. Li, X. Li, P. Huo and W. Shi, *Chin. J. Catal.*, 2021, **42**, 872–903.

130 F. Ahmadijokani, A. Ghaffarkhah, H. Molavi, S. Dutta, Y. Lu, S. Wuttke, M. Kamkar, O. J. Rojas and M. Arjmand, *Adv. Funct. Mater.*, 2024, **34**, 2305527.

131 L. Lu, L. Li, M. Chu, C. Chen, B. Wang, J. Wang, Y. Shen, R. Ma, B. Li, L. Shen, H. Lin and B. Chen, *Adv. Funct. Mater.*, 2025, **35**, 2419433.

132 X. Yu, Y. Hu, X. Luan, S. Jalil Shah, L. Liu, C. Li, Y. Ren, L. Zhou, J. Li, J. Deng, K. Chai, Z. Zhao and Z. Zhao, *Chem. Eng. J.*, 2023, **476**, 146878.

133 J. Li, Y. Jing, S. Zhang, C. Rao, D. Luo, F. Xi, J. Wu, A. He, W. Shen and L. Zhang, *Chem. Eng. J.*, 2024, **499**, 156508.

134 X.-Y. Li, H.-Y. Chu, P. Wang, X.-H. Yi, L. Zhang and C.-C. Wang, *Sep. Purif. Technol.*, 2025, **372**, 133525.

135 S. Zhou, Y. Kuang, H. Yang, L. Gan, X. Feng, C. Mao, L. Chen, J. Zheng and G. Ouyang, *Angew. Chem., Int. Ed.*, 2024, **63**, e202412279.

136 K. Zhao, Z. Zhang, Y. Feng, S. Lin, H. Li and X. Gao, *Appl. Catal., B*, 2020, **268**, 118740.

137 K. Liu, L. Wang, S. Li, H. Liu, D. Zhang, M. Jiang, W. Chen, F. Jiao, X. Zhang and W. Hu, *Adv. Funct. Mater.*, 2023, **33**, 2306871.

138 X. Liu, C. Li, J. Nan, R. Liang, H. Wang, R. Xu and Y. Zhang, *Environ. Sci.: Nano*, 2024, **11**, 1533–1542.

139 Y. Bai, S. Zhang, S. Feng, M. Zhu and S. Ma, *Dalton Trans.*, 2020, **49**, 10745–10754.

140 Z. Tian, Z. Hou, X. Yang, L. Liu and W. Zhang, *Adv. Eng. Mater.*, 2023, **25**, 2201710.

141 M. Govarthanan, R. Mythili, W. Kim, S. Alfarraj and S. A. Alharbi, *J. Hazard. Mater.*, 2021, **414**, 125522.

142 Q. V. Thi, M. S. Tamboli, Q. Thanh Hoai Ta, G. B. Kolekar and D. Sohn, *Mater. Sci. Eng., B*, 2020, **261**, 114678.

143 X.-H. Yi, H. Ji, C.-C. Wang, Y. Li, Y.-H. Li, C. Zhao, A. Wang, H. Fu, P. Wang, X. Zhao and W. Liu, *Appl. Catal., B*, 2021, **293**, 120229.

144 Q. Wen, D. Li, H. Li, M. Long, C. Gao, L. Wu, F. Song and J. Zhou, *Sep. Purif. Technol.*, 2023, **313**, 123518.

145 Y. Zhao, Y. Zhang, X. Cao, J. Li and X. Hou, *Chem. Eng. J.*, 2023, **465**, 143000.

146 Q. Wu, Y. Liu, H. Jing, H. Yu, Y. Lu, M. Huo and H. Huo, *Chem. Eng. J.*, 2020, **390**, 124615.

147 H. Sepehrmansourie, H. Alamgholiloo, N. Noroozi Pesyan and M. A. Zolfigol, *Appl. Catal., B*, 2023, **321**, 122082.

148 R.-X. Mei, P. Wang, F.-X. Wang, Z.-C. Zhang, X.-H. Yi, Z.-Y. Jia, K.-X. Li and C.-C. Wang, *Environ. Res.*, 2025, **279**, 121863.

149 J. Wang, C.-S. Cao, J. Wang, Y. Zhang and L. Zhu, *Appl. Catal., B*, 2022, **304**, 121013.

150 L. Tao, C. Zhou, W. Pan, R. Liu, C. Liao and G. Jiang, *Appl. Catal., B*, 2024, **357**, 124298.

151 M.-Y. Sun, L. Zhang, Y. Li, C.-C. Wang, P. Wang, X. Ren and X.-H. Yi, *Chin. Chem. Lett.*, 2025, **36**, 110035.

152 L. Yuan, C. Zhang, Y. Zou, T. Bao, J. Wang, C. Tang, A. Du, C. Yu and C. Liu, *Adv. Funct. Mater.*, 2023, **33**, 2214627.

153 J. Wang, Y. Mao, R. Zhang, Y. Zeng, C. Li, B. Zhang, J. Zhu, J. Ji, D. Liu, R. Gao and Y. Ma, *Adv. Sci.*, 2022, **9**, 2204036.

154 T. Hu, P. Feng, H. Chu, X. Wang, F. Liu and W. Zhou, *Adv. Funct. Mater.*, 2025, **35**, 2416556.

155 Y. Wu, X. Li, Q. Yang, D. Wang, F. Yao, J. Cao, Z. Chen, X. Huang, Y. Yang and X. Li, *Chem. Eng. J.*, 2020, **390**, 124519.

156 P. Jin, L. Wang, X. Ma, R. Lian, J. Huang, H. She, M. Zhang and Q. Wang, *Appl. Catal., B*, 2021, **284**, 119762.

157 F. Mu, Q. Cai, H. Hu, J. Wang, Y. Wang, S. Zhou and Y. Kong, *Chem. Eng. J.*, 2020, **384**, 123352.

158 L. Shao, Z. Yu, X. Li, X. Li, H. Zeng and X. Feng, *Appl. Surf. Sci.*, 2020, **505**, 144616.

159 W. Lu, C. Wang, W. Song, Z. Zhang, C. Xie and J. Wang, *J. Mater. Chem. A*, 2024, **12**, 20149–20159.

160 S. Li, K. Dong, M. Cai, X. Li and X. Chen, *eScience*, 2024, **4**, 100208.

161 J. Wang, X. Li, B. Zhang and L. Bai, *Inorg. Chem.*, 2023, **62**, 1047–1053.

162 R. Yuan, J. Qiu, C. Yue, C. Shen, D. Li, C. Zhu, F. Liu and A. Li, *Chem. Eng. J.*, 2020, **401**, 126020.

163 X. Liu, Z.-H. Peng, L. Lei, R.-X. Bi, C.-R. Zhang, Q.-X. Luo, R.-P. Liang and J.-D. Qiu, *Appl. Catal., B*, 2024, **342**, 123460.

164 Z. Dong, D. Zeng, Z. Li, J. Chen, Y. Wang, X. Cao, G. Yang, Z. Zhang, Y. Liu and F. Yang, *Chem. Sci.*, 2024, **15**, 19126–19135.

165 C. Gunathilake, I. Soliman, D. Panthi, P. Tandler, O. Fatani, N. A. Ghulamullah, D. Marasinghe, M. Farhath, T. Madhujith, K. Conrad, Y. Du and M. Jaroniec, *Chem. Soc. Rev.*, 2024, **53**, 10900–10969.

166 X. Tao, Y. Zhao, S. Wang, C. Li and R. Li, *Chem. Soc. Rev.*, 2022, **51**, 3561–3608.

167 S. Nishioka, F. E. Osterloh, X. Wang, T. E. Mallouk and K. Maeda, *Nat. Rev. Methods Primers*, 2023, **3**, 42.

168 S. Navalón, A. Dhakshinamoorthy, M. Álvaro, B. Ferrer and H. García, *Chem. Rev.*, 2023, **123**, 445–490.

169 Y. Zhang, D. Ma, J. Li, C. Zhi, Y. Zhang, L. Liang, S. Mao and J.-W. Shi, *Coord. Chem. Rev.*, 2024, **517**, 215995.

170 J. Duan, H. Shabbir, Z. Chen, W. Bi, Q. Liu, J. Sui, L. Đorđević, S. I. Stupp, K. W. Chapman, A. B. F. Martinson, A. Li, R. D. Schaller, S. Goswami, R. B. Getman and J. T. Hupp, *J. Am. Chem. Soc.*, 2023, **145**, 7268–7277.

171 L. Sun, Y. Yuan, F. Wang, Y. Zhao, W. Zhan and X. Han, *Nano Energy*, 2020, **74**, 104909.

172 X. Chen, S. Xiao, H. Wang, W. Wang, Y. Cai, G. Li, M. Qiao, J. Zhu, H. Li, D. Zhang and Y. Lu, *Angew. Chem., Int. Ed.*, 2020, **59**, 17182–17186.

173 Z. Li, J. Zi, X. Luan, Y. Zhong, M. Qu, Y. Wang and Z. Lian, *Adv. Funct. Mater.*, 2023, **33**, 2303069.

174 H. Hu, K. Zhang, G. Yan, L. Shi, B. Jia, H. Huang, Y. Zhang, X. Sun and T. Ma, *Chin. J. Catal.*, 2022, **43**, 2332–2341.

175 J. Dai, L. Yan, W. Yang, R. Li, Y. Dong and Y. Shen, *Appl. Catal., B*, 2025, **362**, 124715.

176 Q.-P. Huang, C. Yang, Q. Yin, A.-A. Zhang, H.-X. Liu, L. Li, M.-M. Liu, Z.-B. Fang and T.-F. Liu, *Angew. Chem., Int. Ed.*, 2025, e202502009.

177 S. Zhang, M. Du, Z. Xing, Z. Li, K. Pan and W. Zhou, *Appl. Catal., B*, 2020, **262**, 118202.

178 J. Guo, Y. Liang, L. Liu, J. Hu, H. Wang, W. An and W. Cui, *Appl. Surf. Sci.*, 2020, **522**, 146356.

179 J. Liu, Q. Li, X. Xiao, F. Li, C. Zhao, Q. Sun, P. Qiao, J. Zhou, J. Wu, B. Li, H. Bao and B. Jiang, *J. Colloid Interface Sci.*, 2021, **590**, 1–11.

180 S. Guo, C.-W. Pan, M. Hou, Y.-T. Hou, S. Yao, T.-B. Lu and Z.-M. Zhang, *Angew. Chem., Int. Ed.*, 2025, **64**, e202420398.

181 H. Yang, C. Yang, N. Zhang, K. Mo, Q. Li, K. Lv, J. Fan and L. Wen, *Appl. Catal., B*, 2021, **285**, 119801.

182 H. Li, H. Gong and Z. Jin, *Appl. Catal., B*, 2022, **307**, 121166.

183 H. Ma, Y. Liu, R. Xiong and J. Wei, *Chin. Chem. Lett.*, 2022, **33**, 1042–1046.

184 Y. Jung, C. W. Lee, B.-H. Lee, Y. Yu, J. Moon, H. S. Lee, W. Ko, J. Bok, K. Lee, J. Lee, M. S. Bootharaju, J. Ryu, M. Kim and T. Hyeon, *J. Am. Chem. Soc.*, 2025, **147**, 1740–1748.

185 Y. Chen, D. Yang, B. Shi, W. Dai, H. Ren, K. An, Z. Zhou, Z. Zhao, W. Wang and Z. Jiang, *J. Mater. Chem. A*, 2020, **8**, 7724–7732.

186 W. Hou, M. Chen, C. Chen, Y. Wang and Y. Xu, *J. Colloid Interface Sci.*, 2021, **604**, 310–318.

187 L. Liu, L. Zuo, X. Zhai, X. Xiao, H. Fan, B. Li and L. Wang, *Appl. Catal., B*, 2025, **361**, 124686.

188 A. Ghosh, S. Karmakar, F. A. Rahimi, R. S. Roy, S. Nath, U. K. Gautam and T. K. Maji, *ACS Appl. Mater. Interfaces*, 2022, **14**, 25220–25231.

189 X. Dai, S. Feng, C. Ma, L. Xu, L. Fan, Z. Ye and Y. Wang, *Appl. Surf. Sci.*, 2023, **639**, 158142.

190 A. Khan, M. Le Pivert, A. Ranjbari, D. Dragoe, D. Bahena-Uribe, C. Colbeau-Justin, C. Herrero, D. Rutkowska-Zbik, J. Deschamps and H. Remita, *Adv. Funct. Mater.*, 2025, 2501736.

191 C.-X. Chen, Y.-Y. Xiong, X. Zhong, P. C. Lan, Z.-W. Wei, H. Pan, P.-Y. Su, Y. Song, Y.-F. Chen, A. Nafady, Sirajuddin and S. Ma, *Angew. Chem., Int. Ed.*, 2022, **61**, e202114071.

192 C. Li, H. Lu, G. Ding, T. Ma, S. Liu, L. Zhang and G. Liao, *Chin. J. Catal.*, 2024, **65**, 174–184.

193 H. Hu, X. Zhang, K. Zhang, Y. Ma, H. Wang, H. Li, H. Huang, X. Sun and T. Ma, *Adv. Energy Mater.*, 2024, **14**, 2303638.

194 Q. Mo, L. Zhang, S. Li, H. Song, Y. Fan and C.-Y. Su, *J. Am. Chem. Soc.*, 2022, **144**, 22747–22758.

195 G.-W. Guan, S.-T. Zheng, M. Xia, K.-X. Li, Y.-S. Ouyang, G. Yang and Q.-Y. Yang, *Chem. Eng. J.*, 2023, **464**, 142530.

196 M. Chen, K. Umer, B. Li, Z. Li, K. Li, W. Sun and Y. Ding, *J. Colloid Interface Sci.*, 2024, **653**, 380–389.

197 S. Mao, J.-W. Shi, G. Sun, D. Ma, C. He, Z. Pu, K. Song and Y. Cheng, *Appl. Catal., B*, 2021, **282**, 119550.

198 S. Mao, J.-W. Shi, G. Sun, Y. Zhang, X. Ji, Y. Lv, B. Wang, Y. Xu and Y. Cheng, *Chem. Eng. J.*, 2021, **404**, 126533.

199 Y.-J. Cheng, J.-Q. Zhao, X.-F. Ma, H.-L. Zheng, L. He, J. Zhang and Q. Lin, *Adv. Mater.*, 2025, 2503756.

200 H. Hu, Z. Wang, L. Cao, L. Zeng, C. Zhang, W. Lin and C. Wang, *Nat. Chem.*, 2021, **13**, 358–366.

201 Q.-C. Lin, W.-M. Liao, J. Li, B. Ye, D.-T. Chen, X.-X. Zhou, P.-H. Li, M. Li, M.-D. Li and J. He, *Angew. Chem., Int. Ed.*, 2025, **64**, e202423070.

202 L. Shiuan Ng, T. Raja Mogan, J.-K. Lee, H. Li, C.-L. Ken Lee and H. Kwee Lee, *Angew. Chem., Int. Ed.*, 2023, **62**, e202313695.

203 M. B. Ross, P. De Luna, Y. Li, C.-T. Dinh, D. Kim, P. Yang and E. H. Sargent, *Nat. Catal.*, 2019, **2**, 648–658.

204 Y. Zhai, P. Han, Q. Yun, Y. Ge, X. Zhang, Y. Chen and H. Zhang, *eScience*, 2022, **2**, 467–485.

205 A. Velty and A. Corma, *Chem. Soc. Rev.*, 2023, **52**, 1773–1946.

206 S. Fang, M. Rahaman, J. Bharti, E. Reisner, M. Robert, G. A. Ozin and Y. H. Hu, *Nat. Rev. Methods Primers*, 2023, **3**, 61.

207 M. Li, Z. Han, Q. Hu, W. Fan, Q. Hu, D. He, Q. Chen, X. Jiao and Y. Xie, *Chem. Soc. Rev.*, 2024, **53**, 9964–9975.

208 D. Li, M. Kassymova, X. Cai, S.-Q. Zang and H.-L. Jiang, *Coord. Chem. Rev.*, 2020, **412**, 213262.

209 P. M. Stanley, V. Ramm, R. A. Fischer and J. Warnan, *Nat. Synth.*, 2024, **3**, 307–318.

210 Z. Cai, H. Liu, J. Dai, B. Li, L. Yang, J. Wang and H. Zhu, *Nat. Commun.*, 2025, **16**, 2601.

211 H. Wu, X. Y. Kong, X. Wen, S.-P. Chai, E. C. Lovell, J. Tang and Y. H. Ng, *Angew. Chem., Int. Ed.*, 2021, **60**, 8455–8459.

212 M. Duflot, C. Marchal, V. Artero, K. C. Christoforidis and V. Keller, *Adv. Energy Mater.*, 2025, 2500104.

213 M. Xu, C. Sun, X. Zhao, H. Jiang, H. Wang and P. Huo, *Appl. Surf. Sci.*, 2022, **576**, 151792.

214 W.-W. Dong, J. Jia, Y. Wang, J.-R. An, O.-Y. Yang, X.-J. Gao, Y.-L. Liu, J. Zhao and D.-S. Li, *Chem. Eng. J.*, 2022, **438**, 135622.

215 Q. Niu, S. Dong, J. Tian, G. Huang, J. Bi and L. Wu, *ACS Appl. Mater. Interfaces*, 2022, **14**, 24299–24308.

216 M. Song, X. Song, X. Liu, W. Zhou and P. Huo, *Chin. J. Catal.*, 2023, **51**, 180–192.

217 S. Li, K. Ji, M. Zhang, C. He, J. Wang and Z. Li, *Nanoscale*, 2020, **12**, 9533–9540.

218 Y. Liu, C. Chen, J. Valdez, D. Motta Meira, W. He, Y. Wang, C. Harnagea, Q. Lu, T. Guner, H. Wang, C.-H. Liu, Q. Zhang, S. Huang, A. Yurtsever, M. Chaker and D. Ma, *Nat. Commun.*, 2021, **12**, 1231.

219 R. Jin, R. Li, M.-L. Ma, D.-Y. Chen, J.-Y. Zhang, Z.-H. Xie, L.-F. Ding, Y. Xie and J.-R. Li, *Small*, 2025, 2409759.

220 N. Li, X.-P. Zhai, B. Ma, H.-J. Zhang, M.-J. Xiao, Q. Wang and H.-L. Zhang, *J. Mater. Chem. A*, 2023, **11**, 4020–4029.

221 L. Xia, W. Zhou, Y. Xu, Z. Xia, X. Wang, Q. Yang, G. Xie, S. Chen and S. Gao, *Chem. Eng. J.*, 2023, **451**, 138747.

222 K. Yuan, K. Tao, T. Song, Y. Zhang, T. Zhang, F. Wang, S. Duan, Z. Chen, L. Li, X. Zhang, D. Zhong, Z. Tang, T.-B. Lu and W. Hu, *J. Am. Chem. Soc.*, 2024, **146**, 6893–6904.

223 B. Li, X. Liu, B. Lei, H. Luo, X. Liu, H. Liu, Q. Gu, J.-G. Ma and P. Cheng, *Adv. Sci.*, 2023, **10**, 2302881.

224 Y. Wang, J.-X. Wei, H.-L. Tang, L.-H. Shao, L.-Z. Dong, X.-Y. Chu, Y.-X. Jiang, G.-L. Zhang, F.-M. Zhang and Y.-Q. Lan, *Nat. Commun.*, 2024, **15**, 8818.

225 S. Karmakar, S. Barman, F. A. Rahimi and T. K. Maji, *Energy Environ. Sci.*, 2021, **14**, 2429–2440.

226 Z. Zhang, Y. Wang, Y. Xie, T. Tsukamoto, Q. Zhao, Q. Huang, X. Huang, B. Zhang, W. Song, C. Chen, H. Sheng and J. Zhao, *Nat. Commun.*, 2025, **16**, 274.

227 H. Dong, X. Zhang, Y. Lu, Y. Yang, Y.-P. Zhang, H.-L. Tang, F.-M. Zhang, Z.-D. Yang, X. Sun and Y. Feng, *Appl. Catal., B*, 2020, **276**, 119173.

228 Y. Ma, Q. Tang, W.-Y. Sun, Z.-Y. Yao, W. Zhu, T. Li and J. Wang, *Appl. Catal., B*, 2020, **270**, 118856.

229 Z. Zhao, J. Bian, L. Zhao, H. Wu, S. Xu, L. Sun, Z. Li, Z. Zhang and L. Jing, *Chin. J. Catal.*, 2022, **43**, 1331–1340.

230 Q. Chen, S. Li, H. Xu, G. Wang, Y. Qu, P. Zhu and D. Wang, *Chin. J. Catal.*, 2020, **41**, 514–523.

231 N. Li, X.-P. Zhai, W.-K. Yan, Y.-J. Zhang, Z.-T. Zhang, M.-J. Xiao, X.-D. Zhang, Q. Wang and H.-L. Zhang, *Sol. RRL*, 2021, **5**, 2100558.

232 Z. Ding, X. Li, C. Kang, S. Yan, D. Zhao, H. Cai, S.-Y. Zhang and Y.-J. Zeng, *Chem. Eng. J.*, 2023, **473**, 145256.

233 H. Yang, G. Liu, L. Zheng, M. Zhang, Z. Guan, T. Liu and J. Yang, *Appl. Catal., B*, 2024, **359**, 124491.

234 L. Wang, J. Mao, G. Huang, Y. Zhang, J. Huang, H. She, C. Liu, H. Liu and Q. Wang, *Chem. Eng. J.*, 2022, **446**, 137011.

235 X.-M. Cheng, P. Wang, S.-Q. Wang, J. Zhao and W.-Y. Sun, *ACS Appl. Mater. Interfaces*, 2022, **14**, 32350–32359.

236 Y. Jiang, Y. Yu, X. Zhang, M. Weinert, X. Song, J. Ai, L. Han and H. Fei, *Angew. Chem., Int. Ed.*, 2021, **60**, 17388–17393.

237 R. R. Ikreedeegh and M. Tahir, *J. Environ. Chem. Eng.*, 2021, **9**, 105600.

238 Y. Yin, S. Feng, X. Xu, Y. Liu, Y. Li, L. Gao, X. Zhou, J. Dong, Y. Wu, J. Su, J.-L. Zuo, S. Yuan and J. Zhu, *J. Am. Chem. Soc.*, 2025, **147**, 16481–16493.

239 S. Xie, Y. Li, B. Sheng, W. Zhang, W. Wang, C. Chen, J. Li, H. Sheng and J. Zhao, *Appl. Catal., B*, 2022, **310**, 121320.

240 E. Cepero-Rodríguez, A. Sousa-Castillo, L. V. Besteiro, B. Puértolas, M. Vázquez-González and M. A. Correa-Duarte, *Adv. Energy Mater.*, 2024, **14**, 2401887.

241 P. Nagababu, Y. T. Prabhu, A. Kularkar, M. S. Subbalakshmi, J. Nagarkar and S. Rayalu, *Emergent Mater.*, 2021, **4**, 503–514.

242 M. A. Baluk, A. Pieczyńska, P. Mazierski, M. Kroczewska, K. Nikiforow, A. Mikolajczyk, J. Dołżonek, J. Łuczak and A. Zaleska-Medynska, *Appl. Catal., B*, 2024, **354**, 124107.

243 S. Dai, T. Kajiwara, M. Ikeda, I. Romero-Muñiz, G. Patriarche, A. E. Platero-Prats, A. Vimont, M. Daturi, A. Tissot, Q. Xu and C. Serre, *Angew. Chem., Int. Ed.*, 2022, **61**, e202211848.

244 Z. Wei, S. Song, H. Gu, Y. Li, Q. Sun, N. Ding, H. Tang, L. Zheng, S. Liu, Z. Li, W. Chen, S. Li and S. Pang, *Adv. Sci.*, 2023, **10**, 2303206.

245 Y. Benseghir, A. Lemarchand, M. Duguet, P. Mialane, M. Gomez-Mingot, C. Roch-Marchal, T. Pino, M.-H. Ha-Thi, M. Haouas, M. Fontecave, A. Dolbecq, C. Sassoye and C. Mellot-Draznieks, *J. Am. Chem. Soc.*, 2020, **142**, 9428–9438.

246 Y.-J. Wang, X. Cheng, N.-N. Ma, W.-Y. Cheng, P. Zhang, F. Luo, W.-X. Shi, S. Yao, T.-B. Lu and Z.-M. Zhang, *Angew. Chem., Int. Ed.*, 2025, **64**, e202423204.

247 F. Dai, M. Zhang, J. Han, Z. Li, S. Feng, J. Xing and L. Wang, *Nano Res.*, 2024, **17**, 1259–1266.

248 R. Manna, S. Rahut and A. N. Samanta, *Mater. Today Energy*, 2023, **35**, 101326.

249 G. Wang, C.-T. He, R. Huang, J. Mao, D. Wang and Y. Li, *J. Am. Chem. Soc.*, 2020, **142**, 19339–19345.

250 N. Li, X. Liu, J. Zhou, W. Chen and M. Liu, *Chem. Eng. J.*, 2020, **399**, 125782.

251 S. Karmakar, S. Barman, F. A. Rahimi, S. Biswas, S. Nath and T. K. Maji, *Energy Environ. Sci.*, 2023, **16**, 2187–2198.

252 W. Guo, K. Zhang, Z. Liang, R. Zou and Q. Xu, *Chem. Soc. Rev.*, 2019, **48**, 5658–5716.

253 L. Li, C. Tang, H. Jin, K. Davey and S.-Z. Qiao, *Chem*, 2021, **7**, 3232–3255.

254 L. Collado, A. H. Pizarro, M. Barawi, M. García-Tecedor, M. Liras and V. A. de la Peña O'Shea, *Chem. Soc. Rev.*, 2024, **53**, 11334–11389.

255 X. Li, L. Tian, Q. Dong, Z. Wang, K. Ralphs, C. Esterhuysen, P. K. J. Robertson, D. W. Bahnemann, G. He and C. Wang, *Coord. Chem. Rev.*, 2025, **534**, 216543.

256 Z. Ding, S. Wang, S. Yan, Y.-J. Zeng and D.-H. Wang, *ChemCatChem*, 2023, **15**, e202201605.

257 C. Wang, S. Wang, Y. Ping, Z. Zhao, D. Guo, D. Wang and X. Bu, *Appl. Catal., B*, 2024, **347**, 123781.

258 S. Mansingh, S. Subudhi, S. Sultana, G. Swain and K. Parida, *ACS Appl. Nano Mater.*, 2021, **4**, 9635–9652.

259 X.-H. Li, H. Li, S.-L. Jiang, L. Yang, H.-Y. Li, Q.-L. Liu, W. Bai, Q. Zhang, C. Xiao and Y. Xie, *ACS Catal.*, 2023, **13**, 7189–7198.

260 J. Qiu, Q. Chen, C. Liu, Y. Chen, J. Wu, K. Jing, J. C. Yu, L. Wu and X. Fu, *Appl. Catal., B*, 2025, **366**, 125034.

261 S. Liu, Z. Teng, H. Liu, T. Wang, G. Wang, Q. Xu, X. Zhang, M. Jiang, C. Wang, W. Huang and H. Pang, *Angew. Chem., Int. Ed.*, 2022, **61**, e202207026.

262 Q. Dong, X. Li, Y. Duan, X. He, X. Liang, F. Yu and C. Wang, *Appl. Catal., B*, 2025, **366**, 125042.

263 H. Ren, J. Tan, Z. Zhao, Y. Shi, X. Xin, D. Yang and Z. Jiang, *Catal. Sci. Technol.*, 2022, **12**, 5540–5548.

264 S. Wang, J.-J. Zhang, M.-Y. Zong, J. Xu, D.-H. Wang and X.-H. Bu, *ACS Catal.*, 2022, **12**, 7960–7974.

265 X. Li, L. Yang, Q. Liu, W. Bai, H. Li, M. Wang, Q. Qian, Q. Yang, C. Xiao and Y. Xie, *Adv. Mater.*, 2023, **35**, 2304532.

266 L. Yuan, C. Tang, P. Du, J. Li, C. Zhang, Y. Xi, Y. Bi, T. Bao, A. Du, C. Liu and C. Yu, *Angew. Chem., Int. Ed.*, 2024, **63**, e202412340.

267 Z. Han, Y. Yang, J. Rushlow, J. Huo, Z. Liu, Y.-C. Hsu, R. Yin, M. Wang, R. Liang, K.-Y. Wang and H.-C. Zhou, *Chem. Soc. Rev.*, 2025, **54**, 367–395.

268 H. Zhang, C. Li, F. Lang, M. Li, H. Liu, D.-C. Zhong, J.-S. Qin, Z. Di, D.-H. Wang, L. Zeng, J. Pang and X.-H. Bu, *Angew. Chem., Int. Ed.*, 2025, **64**, e202418017.

269 G. Hai and H. Wang, *Coord. Chem. Rev.*, 2022, **469**, 214670.

270 S. Yang, B. Pattengale, S. Lee and J. Huang, *ACS Energy Lett.*, 2018, **3**, 532–539.

271 L. Jiao, J. Wang and H.-L. Jiang, *Acc. Mater. Res.*, 2021, **2**, 327–339.

272 C. Li, J. Wang, L. Tong, Y. Wang, P. Zhang, M. Zhu and H. Dong, *Coord. Chem. Rev.*, 2024, **502**, 215623.

273 Y. Fan, H. Zheng, S. Labalme and W. Lin, *J. Am. Chem. Soc.*, 2023, **145**, 4158–4165.

274 T. He, X.-J. Kong and J.-R. Li, *Acc. Chem. Res.*, 2021, **54**, 3083–3094.

275 H. Liu, C. Xu, D. Li and H.-L. Jiang, *Angew. Chem., Int. Ed.*, 2018, **57**, 5379–5383.

276 T. Uekert, C. M. Pichler, T. Schubert and E. Reisner, *Nat. Sustain.*, 2021, **4**, 383–391.

277 A. M. Wright, M. T. Kapelewski, S. Marx, O. K. Farha and W. Morris, *Nat. Mater.*, 2025, **24**, 178–187.

278 W. L. Teo, W. Zhou, C. Qian and Y. Zhao, *Mater. Today*, 2021, **47**, 170–186.

279 D. Chakraborty, A. Yurdusen, G. Mouchaham, F. Nouar and C. Serre, *Adv. Funct. Mater.*, 2024, **34**, 2309089.

280 J. Van Herck, M. V. Gil, K. M. Jablonka, A. Abrudan, A. S. Anker, M. Asgari, B. Blaiszik, A. Buffo, L. Choudhury, C. Corminboeuf, H. Daglar, A. M. Elahi, I. T. Foster, S. Garcia, M. Garvin, G. Godin, L. L. Good, J. Gu, N. Xiao Hu, X. Jin, T. Junkers, S. Keskin, T. P. J. Knowles, R. Laplaza, M. Lessona, S. Majumdar, H. Mashhadimoslem, R. D. McIntosh, S. M. Moosavi, B. Mouriño, F. Nerli, C. Pevida, N. Poudineh, M. Rajabi-Kochi, K. L. Saar, F. Hooriabad Saboor, M. Sagharichiha, K. J. Schmidt, J. Shi, E. Simone, D. Svatunek, M. Taddei, I. Tetko, D. Tolnai, S. Vahdatifar, J. Whitmer, D. C. F. Wieland, R. Willumeit-Römer, A. Züttel and B. Smit, *Chem. Sci.*, 2025, **16**, 670–684.

281 Z. Zheng, N. Rampal, T. J. Inizan, C. Borgs, J. T. Chayes and O. M. Yaghi, *Nat. Rev. Mater.*, 2025, **10**, 369–381.

282 H. Mai, T. C. Le, D. Chen, D. A. Winkler and R. A. Caruso, *Chem. Rev.*, 2022, **122**, 13478–13515.

283 A. Slattery, Z. Wen, P. Tenblad, J. Sanjosé-Orduna, D. Pintossi, T. den Hartog and T. Noël, *Science*, 2024, **383**, eadj1817.

284 Y. Hu, C. Yu, S. Wang, Q. Wang, M. Reinhard, G. Zhang, F. Zhan, H. Wang, D. Skoien, T. Kroll, P. Su, L. Li, A. Chen, G. Liu, H. Lv, D. Sokaras, C. Gao, J. Jiang, Y. Tao and Y. Xiong, *Nat. Catal.*, 2025, **8**, 126–136.

285 J. Castells-Gil, N. Almora-Barrios, B. Lerma-Berlanga, N. M. Padial and C. Martí-Gastaldo, *Chem. Sci.*, 2023, **14**, 6826–6840.

286 M. Bonneau, C. Lavenn, J.-J. Zheng, A. Legrand, T. Ogawa, K. Sugimoto, F.-X. Coudert, R. Reau, S. Sakaki, K.-i. Otake and S. Kitagawa, *Nat. Chem.*, 2022, **14**, 816–822.

287 K. Li, J. Yang and J. Gu, *Acc. Chem. Res.*, 2022, **55**, 2235–2247.